

Deep Learning with Adaptive Hyper-parameters for Low-Dose CT Image Reconstruction

Qiaoqiao Ding, Yuesong Nan, Hao Gao, and Hui Ji

Abstract—Low-dose CT (LDCT) imaging is preferred in many applications to reduce the object’s exposure to X-ray radiation. In recent years, one promising approach to image reconstruction in LDCT is the so-called optimization-unrolling-based deep learning approach, which replaces pre-defined image prior by learnable adaptive prior in some model-based iterative image reconstruction scheme (MBIR). While it is known that setting appropriate hyper-parameters in MBIR is challenging yet important to the reconstruction quality, it does not receive enough attention in the development of deep learning methods. This paper proposed a deep learning method for LDCT reconstruction that unrolls a half-quadratic splitting scheme. The proposed method not only introduces learnable image prior built on framelet filter bank, but also learns a network that automatically adjusts the hyper-parameters to fit noise level and the data for processing. As a result, only one universal model needs to be trained in our method to process the data taken under different dose levels. Experimental evaluation on clinical patient dataset showed that the proposed method outperformed both conventional and deep-learning-based solutions by a large margin.

Index Terms—X-ray CT, Image reconstruction, Low Dose CT, Deep Neural Networks

I. INTRODUCTION

X-RAY Computed Tomography (CT) is to provide high-resolution three-dimensional (3D) images of internal anatomical structures using X-ray scanning and computational tomographic imaging techniques. As excessive exposure to radiation from X-ray CT scanner may increase the risk of damage to issue, many techniques have been developed to use less radiation than conventional CT scan, including decreasing the number of projection views [1] and lowering the X-ray tube current [2]. The latter is the so-called low-dose CT (LDCT). As a result, the signal-to-noise ratio (SNR) of the measurements collected is much lower than that of conventional CT, which has a negative impact on the quality of the reconstructed image.

Given measurements from LDCT with low SNR, the images reconstructed by conventional filtered back-projection (FBP) method are often of poor quality with noticeable artifacts. In such a setting, the so-called model-based iterative reconstruction (MBIR) methods [3], [4] are more widely used for image reconstruction. In MBIR, image reconstruction is usually formulated as an optimization problem regularized by certain

functional for suppressing noise magnification during reconstruction. Such a regularization term is derived from some pre-defined prior on the image. In the past, many different priors have been proposed for MBIR-based reconstruction, *e.g.* total variation (TV) [5]–[7], wavelet-based sparsity prior [8], [9], nonlocal sparsity prior [10], and low-rank-based patch prior [11]–[14]. The resulting optimization problems from these MBIR-based methods usually require some iterative scheme to find an approximate solution. Instead of using some man-crafted prior for regularization, there are also some works that learn image prior for regularization, *e.g.*, dictionary learning [15] and sparsifying transform learning [16]. In recent years, there has been a rapid progress on the development of deep learning methods for image reconstruction in LDCT. Most existing methods, *e.g.* [17]–[19], are based on the so-called optimization unrolling, which replaces the step involving the image prior by a learnable function built on a deep neural network (NN). The performance of these optimization-unrolling-based deep learning methods is very promising in LDCT image reconstruction.

For MBIR, there are usually several hyper-parameters involved in the iterative scheme. It is known that in addition to the choice of image prior, the setting of these hyper-parameters also plays an important role in the reconstruction; see [15], [20], [21]. In other words, how to automate the selection of appropriate hyper-parameters is an important yet challenging task in MBIR. The optimal values of these hyper-parameters depend on many factors [20]–[25], including:

- SNR of measurement data;
- Content of target image for reconstruction;
- Global convergence property and fast convergence rate.

Based on these factors, there has been an enduring effort on developing automatic selection strategies of hyper-parameters for the classic non-learning-based regularization methods, *e.g.* [16], [20], [22]–[25].

Similar to classic MBIR-based approaches, there are also several hyper-parameters involved in existing optimization-unrolling-based deep learning methods, which are either manually tuned-up [17], [26] or treated as one part of network weights to be learned during the training [18], [19], [27]. As a result, the setting of these hyper-parameter is optimized only for one specific noise level of measurement data. When processing the data with different noise levels, they need to train different networks w.r.t. different noise levels. Such a practice can be inconvenient and sometimes difficult in practical usage when noise level of data is unknown. Furthermore, these hyper-parameters are fixed as constants for different

Q. Ding* (e-mail: matding@nus.edu.sg), Y. Nan* (e-mail: matny@nus.edu.sg), and H. Ji* (e-mail: matjh@nus.edu.sg) are with Department of Mathematics, National University of Singapore. 119076, SINGAPORE

H. Gao† (e-mail: hao.gao.2012@gmail.com) is with Department of Radiation Oncology, Winship Cancer Institute of Emory University, 30322, USA

measurements which correspond to the images with different contents. Such a constant treatment on hyper-parameters in existing deep learning methods [17], [28] certainly is not optimal. Motivated by the practical value of processing data with unknown noise level and the need for better image quality in LDCT imaging, this paper aims at developing an adaptive and automated hyper-parameter selection mechanism in deep-learning-based image reconstruction methods, as well as other refinements for further performance improvement.

In this paper, we proposed an image reconstruction method in LDCT whose image prior and hyper-parameter selection are collaboratively learned by two NNs. The proposed method is based on the unrolling of the so-called half-quadratic splitting method [29]. Specifically, the proposed NN is composed by K stages, which corresponds to K outer iterations in the optimization method. Each stage contains two blocks:

- **Inversion block** reconstructs an image using both the measurement and the estimate from the previous stage, whose hyper-parameters are predicted by a multi-layer perception neural network (MLP).
- **De-noising block** removes the artifacts of the estimate passed from the inverse block by a convolutional neural network (CNN).

The de-noising block, same as many existing approaches, is implemented using a CNN. However, the design of inversion block is less attentive yet crucial. In a nutshell, we are focusing on the construction of a powerful inversion block which enables the adaption to both noise level and image contents. The main difference is highlighted as follows:

- Hyper-parameters involved inner-loop is predicted by a learnable NN for the adaptivity of both dose levels and image contents.
- Fine-grained high-pass filter bank is adopted instead of often-seen gradient operator or learnable filter bank for better sub-band reconstruction and image content adaption.

Extensive experimental studies showed these designs not only bring performance advantage in LDCT image reconstruction, in compared with existing methods by a large margin, but also allows one to train a single NN model to process the data with unknown dose level.

A. Related work

Due to space limitation, we only discuss most related methods for LDCT image reconstruction, *e.g.*, deep-learning-based methods. One type of such methods uses deep NN to post-process the images reconstructed from some existing methods. By treating the artifacts as noise in the reconstructed images, these methods train an NN-based image denoiser to remove the artifacts from images for better quality. The denoising NN is trained by using the pairs of the image reconstructed from LDCT and its counterpart from conventional CT. Different NN architectures have been proposed for such a denoiser, *e.g.*, CNN [30], residual encoder CNN [31], residual network [32], [33], U-net [32], [34], GAN [35], [36], multi-resolution deep convolutional framelets neural network [37]. Instead of directly denoising images, Kang *et al.* [38], [39]

proposed to denoise wavelet transform coefficients of the images using an NN-based denoiser. Overall, in such a post-processing approach, deep learning does not get involved in the reconstruction and data consistence is omitted.

In recent years, a more popular deep-learning-based approach is built on optimization unrolling, which introduces NNs in the iterations of the MBIR by replacing image-prior-based operations with the function modeled using learnable NN [40]. In other words, the pre-defined image prior is replaced by a learnable prior using NN. There are two ways to train the NN. One is plugging a pre-trained NN into the iterations of some MBIR; see *e.g.* [17], [28]. The other is training the end-to-end NNs together with the MBIR; see *e.g.* [18], [19], [27], [41]–[45].

In addition to the training scheme, another main difference among different optimization-unrolling-based deep learning methods lies in what numerical solver is chosen for unrolling. Based on the alternating direction method of multipliers (ADMM), the ADMM-net is proposed in [27] for image reconstruction in compressed-sensing-based Magnetic Resonance Imaging (MRI). For consistent CT image reconstruction, Gupta *et al.* [17] proposed to unroll the proximal gradient methods with CNN-based learnable prior. For LDCT image reconstruction, the ADMM is used in [18] and the primal-dual hybrid gradient (PDHG) method is used in [19] for unrolling with learnable image prior.

Similar to most iterative schemes of MBIR, how to set appropriate hyper-parameters is very crucial to the quality of reconstructed images in these optimization-unrolling-based deep learning methods; see *e.g.* [17], [28]. Different from conventional methods, there are few systematic studies that address the problem of hyper-parameter setting in deep learning methods for image reconstruction.

In existing deep learning methods, the hyper-parameters are either manually tuned-up [17], [28] or treated as a part of learnable NN parameters [18], [19]. Both treatments are sub-optimal. The former can only take a few trials on the hyper-parameters, since training the NN is a very time-consuming process. The later usually cannot find optimal values for hyper-parameters either, as these hyper-parameters are treated the same as millions of other NN weights in the optimization. In addition, for measurement with different dose levels, these deep learning methods need to train different models to fit a specific noise level for optimal performance. There will be a performance hit if only one model is trained for processing the data with different dose levels.

II. MEASUREMENT MODEL AND PROBLEM FORMULATION

In CT imaging with a mono-energetic source, the projection measurements from CT scan follow the Poisson distribution [46], which can be expressed as:

$$\bar{y}_i \sim \text{Poisson}\{I_i \exp(-[\mathbf{A}\mathbf{x}]_i)\} + \mathcal{N}(0, \sigma_e^2), \quad (1)$$

where $\bar{\mathbf{y}} = [\bar{y}_i]_{i=1}^{N_d}$ represents the vector of measured projections. I_i represents the incident X-ray intensity incorporating X-ray source illumination and the detector efficiency. $\mathbf{A} = [a_{i,j}]_{i,j}$ is the $N_d \times N_p$ system matrix, and $\mathbf{x} = [x_j]_{j=1}^{N_p}$ denotes

the attenuation map. The quantity $[\mathbf{Ax}]_i = \sum_{j=1}^{N_p} a_{ij}x_j$ refers to the line integral of the attenuation map \mathbf{x} along the i -th X-ray. \mathcal{N} refers to normal distribution, and the quantity σ_e^2 denotes the variance of the background electronic noise which is considered to be stable for a commercial CT scanner and has been converted to photon units [47].

It is noted that the noise level varies for different target images. Given a target image \mathbf{x} , its noise level is controlled by I_i , *i.e.*, the measure data is corrupted with noise which becomes larger when dose level I_i decreases. However, even with a fixed dose level I_i , for different patients or different parts of human-body, their corresponding noise levels are different too.

To reconstruct the attenuation map \mathbf{x} , one can first run the correction and the logarithm transform on the noisy measurements $\bar{\mathbf{y}}$ to generate the so-called sinogram $\mathbf{y} = [y_i]_{i=1}^{N_d}$, whose relation to \mathbf{Ax} is often expressed as:

$$\mathbf{y} = \mathbf{Ax} + \epsilon, \quad (2)$$

where $\epsilon = \mathcal{N}(0, \sigma^2)$ denotes the noise. The linear system (2) is ill-posed, and certain regularization needs to be imposed to resolve the solution ambiguity and suppress noise magnification. Let $p(\mathbf{x}; \lambda)$ denotes the prior distribution function of \mathbf{x} with distribution parameter λ . The maximum a posteriori (MAP) estimation of \mathbf{x} is then the minimum of the cost function given by

$$\min_{\mathbf{x}} \frac{1}{2} \|\mathbf{Ax} - \mathbf{y}\|_{\sigma^2}^2 - \log p(\mathbf{x}; \lambda), \quad (3)$$

where the first is data fidelity term and the second is regularization term on \mathbf{x} derived from its prior distribution. The model (3) is often called penalized weighted least-squares (PWLS) image reconstruction model [3], [48], [49], which is a widely used one in CT image reconstruction.

Many regularization terms $-\log p(\mathbf{x}; \lambda)$ have been proposed for LDCT image reconstruction, *e.g.* TV [6], nonlocal TV [10] and framelet [8]. These regularization functionals are usually not directly defined in image domain, but in the domain of image gradients or their generalizations. For example, both the TV and wavelet-transform-based regularizations take the form of $\lambda \|\Gamma \mathbf{x}\|_1$, where Γ is the gradient operator ∇ (TV) or wavelet transform W (wavelet). The prior distribution parameter λ is also called the regularization parameter, which needs to be set in advance.

There are many numerical scheme for solving (3) with $-\log(p(\mathbf{x}; \lambda)) = \lambda \rho(\Gamma \mathbf{x})$, *e.g.* ADMM and PDHG. In this paper, our work is based on the half-quadratic splitting method [29], which solve the problem (3) by introducing an auxiliary variable \mathbf{z} with following two steps:

$$\textbf{Inversion: } \mathbf{x}^k = \arg \min_{\mathbf{x}} \frac{1}{\sigma^2} \|\mathbf{Ax} - \mathbf{y}\|_2^2 + \frac{1}{\sigma_1^k} \|\Gamma \mathbf{x} - \mathbf{z}^k\|_2^2, \quad (4a)$$

$$\textbf{Denoising: } \mathbf{z}^{k+1} = \arg \min_{\mathbf{z}} \lambda \rho(\mathbf{z}) + \frac{1}{\sigma_1^k} \|\Gamma \mathbf{x}^k - \mathbf{z}\|_2^2, \quad (4b)$$

where $\{\sigma_1^k\}_k$ is the parameter sequences of the algorithm. The noise variance σ , the hyper-parameters $\{\sigma_1^k\}_k$, and the regularization parameter λ , will make a noticeable impact on the convergence behavior and the quality of the result.

There are two blocks in the iterative scheme (4). The first is an inversion block (4a), which reconstructs an image from the measurement \mathbf{y} and the estimate from the previous iteration. The second is a denoising block (4b), which refines the estimate from the inverse block using the prior-based regularization. The performance of the scheme (4) depends on the answers to the following two questions.

- 1) What prior $p(\mathbf{x}; \lambda)$ fits the target image \mathbf{x} well?
- 2) What values of the hyper-parameters are optimal for estimating \mathbf{x} ?

Most existing optimization-unrolling-based methods focus on the replacement of the denoising block (4b) using a NN-based denoiser to address the first problem. However, the second problem has not attracted much attention in spite of the importance of the hyper-parameters [17]. The current treatment on the setting of hyper-parameters is done by either manual selection or learning them as one part of NN weights.

This paper aims at designing a deep learning method for LDCT reconstruction that not only uses a CNN-based denoiser to replace (4b), but also introduces a MAP-based predictor in the inversion block (4a) to automate the adaptive setting of hyper-parameters to the SNR of measurement data and the target image \mathbf{x} . The proposed deep learning method not only provides very competitive performance for LDCT image reconstruction, but also is universal such that a single trained NN model can be used for the reconstruction of CT measurements with varying dose levels.

III. METHOD

In this section, we give a detailed discussion on the proposed deep learning method for LDCT reconstruction.

A. Detailed algorithm of the iterative scheme (4)

Recall that each iteration of the scheme (4) has two blocks: inversion block and denoising block. For the inversion block, the problem has an analytical solution given by

$$\mathbf{x}^k = (\mathbf{A}^\top \mathbf{A} + \frac{\sigma^2}{\sigma_1^k} \Gamma^\top \Gamma)^{-1} (\mathbf{A}^\top \mathbf{y} + \frac{\sigma^2}{\sigma_1^k} \Gamma^\top \mathbf{z}^k).$$

In conventional methods such as TV method, the operator Γ is image gradient operator ∇ that convolves the image \mathbf{x} by two filters: $[1, -1]$ and $[1, -1]^\top$. Motivated by the performance improvement of framelet transform over ∇ in many image recovery tasks, we propose to use the filter bank of spline framelet transform [50]. In our implementation, the filter bank of linear B-spline framelet transform is adopted, which contains totally 8 2D high-pass filters

$$\{\mathbf{f}_i\}_{i=1}^8 := \{h_{k_1} h_{k_2}^\top\}_{0 \leq k_1, k_2 \leq 2} \setminus \{h_0 h_0^\top\}, \quad (5)$$

composed by the tensor product of three 1D filters:

$$h_0 = [\frac{1}{4}, \frac{1}{2}, \frac{1}{4}]^\top, h_1 = [-\frac{1}{4}, \frac{1}{2}, \frac{1}{4}]^\top, h_2 = [\frac{\sqrt{2}}{4}, 0, -\frac{\sqrt{2}}{4}]^\top. \quad (6)$$

It can be seen that such a filter bank is composed of more fine-grained 2D filters on image gradients with various difference orders and along different directions. Then, the iterative

scheme (4) can be re-formulated as

$$\begin{aligned} \mathbf{x}^k &= \arg \min_{\mathbf{x}} \|\mathbf{A}\mathbf{x} - \mathbf{y}\|_2^2 + \sum_{i=1}^L \beta_i^k \|\mathbf{f}_i \otimes \mathbf{x} - \mathbf{z}_i^k\|_2^2, \\ \mathbf{z}_i^{k+1} &= \arg \min_{\mathbf{z}_i} \|\mathbf{f}_i \otimes \mathbf{x}^k - \mathbf{z}_i\|_2^2 + \alpha^k \rho(\mathbf{z}_i), \quad 1 \leq i \leq L, \end{aligned} \quad (7)$$

where $\beta_i^k = \frac{\sigma^2}{\sigma_i^k}$, $\alpha_i^k = \frac{1}{\lambda_i \sigma_i^k}$. Again, the inversion block (7) has an analytical solution expressed by

$$\mathbf{x}^k = \left(\mathbf{A}^\top \mathbf{A} + \sum_{i=1}^L \beta_i^k \mathbf{F}_i^\top \mathbf{F}_i \right)^{-1} \left(\mathbf{A}^\top \mathbf{y} + \sum_{i=1}^L \beta_i^k \mathbf{F}_i^\top \mathbf{z}_i^k \right), \quad (9)$$

where \mathbf{F}_i denote the matrix form of the convolution operator with the filter \mathbf{f}_i .

In short, the inversion block (7) reconstructs \mathbf{x} from measurement data \mathbf{y} and the estimate of $\{\mathbf{z}_i\}_{i=1}^L$ in high-pass channels using the least squares estimator, and the denoising block (8) refines the estimate of $\{\mathbf{z}_i\}_{i=1}^L$ in high-frequency channels by treating the artifacts as noise and suppressing it via imposed regularization.

B. Inversion block with an MLP-based adaptive predictor for hyper-parameters

Recall that in the analytical solution of the inversion block (9), there is a sequence of hyper-parameters $\{\beta_i^k\}_{i=1}^L$. The setting of such a sequence makes significant impact on the intermediate output, which in turn makes noticeable impact on the quality of the final result. In this section, we present a NN-based solution to predict $\{\beta_i^k\}_{i=1}^L$ for optimal performance.

Indeed, the step (7) can be interpreted as an MAP estimator under the assumption that both \mathbf{y} and $\{\mathbf{z}_i\}_{i=1}^L$ are the measurements of $\mathbf{A}\mathbf{x}$ and $\mathbf{F}_i\mathbf{x}$ corrupted by additive Gaussian white noise:

$$\begin{cases} \mathbf{y} - \mathbf{A}\mathbf{x} = \mathbf{n} \sim \mathcal{N}(0, \sigma^2), \\ \mathbf{z}_i^k - \mathbf{F}_i\mathbf{x} = \epsilon_i^k \sim \mathcal{N}(0, (\sigma_i^k)^2), \quad 1 \leq i \leq L. \end{cases} \quad (10a)$$

$$(10b)$$

In such a simplified case, one can have an explicit solution to the hyper-parameters: $\beta_i^k := (\sigma_i^k)^{-2} \sigma^2$. Such an observation is also utilized in [51] for automating the setting of hyper-parameters.

In above formula, the ground truth \mathbf{x} is unknown, which hinders the estimation of hyper-parameters sequence $\{\beta_i^k\}$. Our observation is that for unrolling-based framework, the estimated intermediate reconstruction results \mathbf{x}^{k-1} can serve as surrogates for unknown ground truth \mathbf{x} in stage k . Mathematically, such approximation can be done via

$$\begin{cases} \mathbf{n} = \mathbf{y} - \mathbf{A}\mathbf{x}^{k-1} + \mathbf{A}\delta^{k-1}, \\ \epsilon_i^k = \mathbf{z}_i^k - \mathbf{F}_i\mathbf{x}^{k-1} + \mathbf{F}_i\delta^{k-1}, \quad 1 \leq i \leq L. \end{cases} \quad (11a)$$

$$(11b)$$

with error $\delta^{k-1} = \mathbf{x}^{k-1} - \mathbf{x}$. By taking the ℓ_2 norm, the parameters $\{\sigma^2, (\sigma_i^k)^2\}$ can be estimated from the following relationship,

$$\begin{cases} \sigma^2 = N_d \mathbf{h}_0(\|\mathbf{y} - \mathbf{A}\mathbf{x}^{k-1}\|_2^2) \\ (\sigma_i^k)^2 = N_p \mathbf{h}_i(\|\mathbf{z}_i^k - \mathbf{F}_i\mathbf{x}^{k-1}\|_2^2), \quad 1 \leq i \leq L. \end{cases} \quad (12a)$$

$$(12b)$$

where $\{\mathbf{h}_i\}_{i=0}^L$ denotes the correction functions that rectify the input ℓ_2 norm of the residues due to the presence of unknown error δ^{k-1} . Thus, the parameters can be estimated via

$$\beta_i^k = \frac{\sigma^2}{(\sigma_i^k)^2} = \frac{N_d \mathbf{h}_0(\|\mathbf{y} - \mathbf{A}\mathbf{x}^{k-1}\|_2^2)}{N_p \mathbf{h}_i(\|\mathbf{z}_i^k - \mathbf{F}_i\mathbf{x}^{k-1}\|_2^2)}, \quad 1 \leq i \leq L \quad (13)$$

Instead of direct modeling $\{\mathbf{h}_i\}_{i=0}^L$, we choose a non-linear function, MLP, to model such relationship for simplicity, *i.e.* we automate the estimation of the hyper-parameter sequence $\{\beta_i^k\}$ using a learnable NN. By setting $\mathbf{r}_0^k = \mathbf{y} - \mathbf{A}\mathbf{x}^{k-1}$ and $\mathbf{r}_i^k = \mathbf{z}_i^k - \mathbf{F}_i\mathbf{x}^{k-1}$, the NN, denoted by $\mathcal{P}_{\text{mlp}}(\cdot; \theta_P^k)$ with parameters θ_P^k , takes the known value $\{\|\mathbf{r}_i^k\|\}_{i=0}^L$ as the input and outputs the estimation of $\{\beta_i^k\}$:

$$\mathcal{P}_{\text{mlp}}(\cdot, \theta_P^k) : [\|\mathbf{r}_i^k\|_2]_{i=0}^L \in \mathbb{R}^{L+1} \rightarrow [\beta_i^k]_{i=1}^L \in \mathbb{R}^L. \quad (14)$$

An MLP is implemented for modeling the mapping \mathcal{P}^k , which contains 3 layers. Each layer is composed by one fully connected layer followed by one ReLU function. See Fig. 1 for the diagram of the proposed hyper-parameter predictor \mathcal{P}^k .

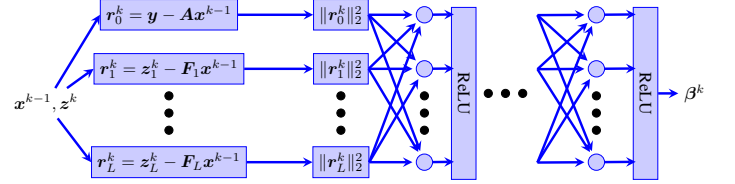


Fig. 1: Diagram of the MLP for predicting hyper-parameter sequence $\beta^k = \{\beta_i^k\}_{i=1}^L$.

Once the sequence $\{\beta_i^k\}_{i=1}^L$ is predicted, we can update the estimate using the analytical solution (9). We denote such a solution by

$$\mathcal{I}_{\text{inv}}^k : [\mathbf{y}, \{\beta_i^k\}_{i=1}^L, \{\mathbf{z}_i^k\}_{i=1}^L] \rightarrow \mathbf{x}^k. \quad (15)$$

In summary, the inversion block can be expressed as

$$\mathcal{L}^k(\cdot; \theta_P^k) : [\mathbf{y}, \{\mathbf{z}_i^k\}_{i=1}^L] \rightarrow \mathbf{x}^k, \quad (16)$$

where θ_P^k is the learnable weights.

Note that one can numerically solve (9) by conjugate gradient. To give the backward gradient for the backpropagation algorithm, let $\ell : \mathbb{R}^{N_P} \rightarrow \mathbb{R}$, then the derivatives of $\ell(\mathbf{x}^k)$ with respect to $\{\beta_i^k\}_{i=1}^L, \{\mathbf{z}_i^k\}_{i=1}^L$ can be correspondingly computed by:

$$\frac{\partial \ell(\mathbf{x}^k)}{\partial \mathbf{z}_i^k} = \beta_i^k \mathbf{F}_i (\mathbf{A}^\top \mathbf{A} + \sum_{i=1}^L \beta_i^k \mathbf{F}_i^\top \mathbf{F}_i)^{-1} \frac{\partial \ell(\mathbf{x}^k)}{\partial \mathbf{x}^k}, \quad (17a)$$

$$\frac{\partial \ell(\mathbf{x}^k)}{\partial \beta_i^k} = (\mathbf{F}_i^\top \mathbf{z}_i^k - \mathbf{F}_i^\top \mathbf{F}_i \mathbf{x}^k)^T (\mathbf{A}^\top \mathbf{A} + \sum_{i=1}^L \beta_i^k \mathbf{F}_i^\top \mathbf{F}_i)^{-1} \frac{\partial \ell(\mathbf{x}^k)}{\partial \mathbf{x}^k}. \quad (17b)$$

C. Denoising block with CNN-based adaptive prior

For the denoising block, following many existing methods, we also adopt a CNN to learn the function (8) such that the estimate passed from the inversion block can be refined using learnable prior that is adaptive to the target image. It is

noted that the measurements of an image in different high-pass channels are highly correlated. Independently running denoising in these high-pass channels is not a good practice as the inherent correlation is lost in such a process. Thus, the proposed CNN take the estimate \mathbf{x}^k as the input and output a denoised version $\tilde{\mathbf{x}}^k$, which is then fed to L high-pass channels to have an estimate \mathbf{z}_i^{k+1} :

$$\mathbf{z}_i^{k+1} = \{\mathbf{f}_i \otimes \tilde{\mathbf{x}}^k\}_i, \quad 1 \leq i \leq L. \quad (18)$$

Such a procedure reserves the correlations of an image among different high-pass channels.

Furthermore, instead of only taking the previous estimate \mathbf{x}^k as the input, The CNN for denoising block takes all previous estimates $\{\mathbf{x}^0, \mathbf{x}^1, \dots, \mathbf{x}^k\}$ as the input, which can alleviate the so-called vanishing gradient in training [52]. Another benefit of doing so is that the fusion of these previous estimates provide more information for the refinement, as these are different estimates of the truth with different types of artifacts. The final version of the mapping of the CNN-based denoising process can be expressed as

$$\mathcal{D}_{\text{cnn}}^k(\cdot, \theta_D^k) : [\mathbf{x}^0, \mathbf{x}^1, \dots, \mathbf{x}^k] \rightarrow \tilde{\mathbf{x}}^k, \quad (19)$$

where θ_D^k denotes the parameters of denoising NN, $\mathcal{D}_{\text{cnn}}^k$. The output of the whole denoising block is then

$$\mathbf{z}_i^{k+1} = \mathbf{f}_i \otimes \mathcal{D}_{\text{cnn}}^k([\mathbf{x}^0, \mathbf{x}^1, \dots, \mathbf{x}^k], \theta_D^k). \quad (20)$$

For each stage of the iteration, we use 17-block standard CNN with the structure Conv \rightarrow BN \rightarrow ReLU, except the first block and the last block. The BN layer is omitted for the first and last block. For all the Conv layers in the CNN, the kernel size is set as 3×3 . The channel size is set to 64. See Fig. 2 for the diagram of the CNN-based denoising block. In summary, the denoising block can be expressed as

$$\mathcal{D}^k(\cdot; \theta_D^k) : [\mathbf{x}^0, \mathbf{x}^1, \dots, \mathbf{x}^k] \rightarrow \mathbf{z}^{k+1}, \quad (21)$$

where θ_D^k is the set of learnable weights w.r.t. the CNN-based denoiser.

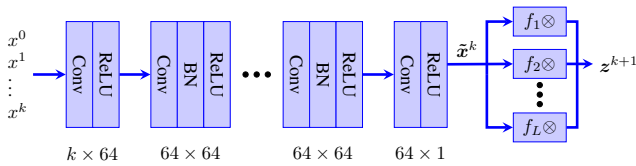


Fig. 2: Diagram of the CNN for denoising.

D. The overall architecture of the proposed method

The proposed deep learning method for LDCT contains totally $K + 1$ stages, denoted by $\{\mathcal{S}^k\}_{k=0}^K$. Let \mathcal{L}^k and \mathcal{D}^k denote the inversion block and denoising block defined by (16) and (21). Then, each stage corresponds to one iteration in MBIR as follows.

$$\mathcal{S}^0(\cdot; \Theta^0) : \quad \mathbf{y} \xrightarrow{\mathcal{L}^0} \mathbf{x}^0, \quad (22)$$

$$\mathcal{S}^k(\cdot; \Theta^k) : \quad [\mathbf{y}, \{\mathbf{x}^\ell\}_{\ell=0}^{k-1}] \xrightarrow{\mathcal{D}^{k-1}} [\mathbf{y}, \mathbf{z}^{k-1}] \xrightarrow{\mathcal{L}^k} \mathbf{x}^k, \quad (23)$$

for $k = 1, 2, \dots, K$, where $\Theta^k := \{\theta_{\mathcal{D}}^{k-1}, \theta_{\mathcal{P}}^k\}$ denotes the weights at the k -th stage, including the weights of $\mathcal{D}_{\text{cnn}}^{k-1}$, and $\mathcal{P}_{\text{mlp}}^k$. In stage \mathcal{S}^0 , we initialize $\mathbf{z}^0 = \mathbf{0}$ and $\beta_i^0 = 0.005$ for $1 \leq i \leq L$. It can be seen that when the measurement is fed to the proposed NN, it generates a sequence through the $K + 1$ stages:

$$\{\mathbf{x}^0, \mathbf{x}^1, \dots, \mathbf{x}^K\},$$

The final output of the whole NN is defined as $\mathbf{x}^* := \mathbf{x}^K$. See Fig. 3 for the outline of the proposed NN, termed as *AHP-Net*, for LDCT reconstruction.

For the training of the proposed AHP-Net, we consider the training dataset $\{\mathbf{x}_j, \mathbf{y}_j\}_{j=1}^J$ with J training samples, where each $(\mathbf{x}_j, \mathbf{y}_j)$ denotes one pair of normal dose image and low dose sinogram data. The loss function is defined as

$$\mathcal{L}(\Theta) = \frac{1}{J} \sum_{j=1}^J \left(\|\mathbf{x}_j^K - \mathbf{x}_j\|_2^2 + \sum_{k=1}^{K-1} \mu_k \|\mathbf{x}_j^k - \mathbf{x}_j\|_2^2 \right), \quad (24)$$

where $\Theta := \{\Theta^k\}_{k=0}^K$ is the whole set of NN parameters, and

$$\mathbf{x}_j^k = (\mathcal{S}^k(\cdot; \Theta^k) \circ \mathcal{S}^{k-1}(\cdot; \Theta^{k-1}) \circ \dots \circ \mathcal{S}^0(\cdot; \Theta^0))(\mathbf{y}_j)$$

denotes the output of the AHP-Net at the k -th stage w.r.t. the input \mathbf{y}_j . The first term in (24) is for encouraging the output of the NN close to the truth. The second term is for ensuring the intermediate results not too far from the truth. The balancing parameters $\{\mu_k\}_{k=1}^{K-1}$ are set to $\frac{4}{5}$ throughout all experiments. Our optimization was done via minimizing the loss function (24) using the Adam method. Once we finished the training of the model, an estimation of NN parameters $\bar{\Theta}$ is obtained. For a low dose input data \mathbf{y} , the image can be reconstructed by fed it into the NN with parameters $\bar{\Theta}$:

$$\mathbf{x}^* := (\mathcal{S}^k(\cdot; \bar{\Theta}^k) \circ \mathcal{S}^{k-1}(\cdot; \bar{\Theta}^{k-1}) \circ \dots \circ \mathcal{S}^0(\cdot; \bar{\Theta}^0))(\mathbf{y}).$$

E. Implementation

The proposed AHP-Net is implemented with $K = 3$ stages. For the proposed NN method, training is performed with PyTorch [53] framework on a NVIDIA Titan GPU. As for parameters in the Adam optimizer, we set momentum parameter $\beta = 0.9$, mini-batch size to be 4, and the learning rate to be 10^{-4} . The model was trained for 50 epochs. The convolution weight of \mathcal{D}_{cnn} for denoising were initialized with orthogonal matrices and the biases were initialized with zeros. All weights in \mathcal{P}_{mlp} were initialized to 1 and the biases to 0.

IV. EXPERIMENTS

In this section, we conduct a comprehensive experimental evaluation of the proposed AHP-Net, and compare it to other representative methods in LDCT image reconstruction.

A. Dataset for evaluation

To evaluate the performance of the proposed method under different dose levels, we simulated low dose projection data from their normal-dose counterparts. The normal dose dataset included 6400 normal-dose prostate CT images of 256×256 pixels per image from 100 anonymized scans, where 80%, and

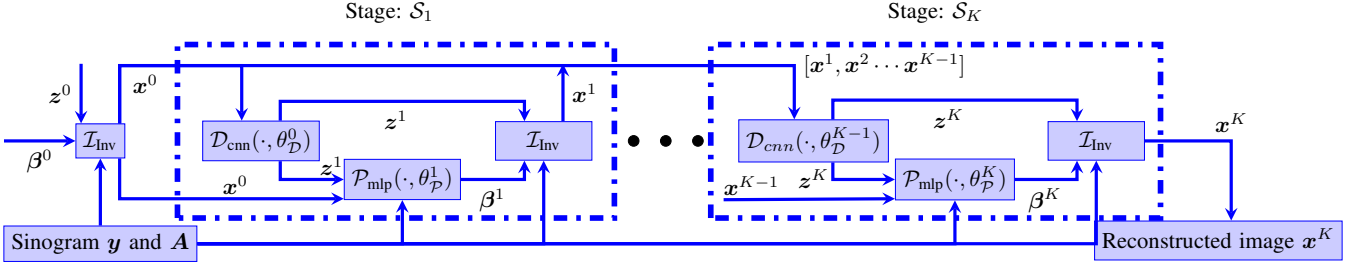


Fig. 3: Diagram of the proposed AHP-Net for LDCT image reconstruction.

20% of the data is set for training and testing respectively. The LDCT projection data was simulated by adding Poisson noise onto the normal-dose projection data as Section II. The simulated geometry for projection data includes fan-beam CT scanner, flat-panel detector of $0.388 \text{ mm} \times 0.388 \text{ mm}$ pixel size, 600 projection views evenly spanning a 360° circular orbit, 512 detector bins for each projection with 1 mm pixel size, 100.0 cm source to detector distance, and 50.0 cm source to isocenter distance.

For the training dataset, 80 patients' simulated low-dose projection and corresponding normal dose images were selected as the pairs of measurement and truth image. For every patient's normal dose data, we simulated the low-dose measurement with uniform dose level. Then, the sinograms of different patients were obtained by taking logarithm on projection data \bar{y} . The remaining 20 scans were selected as testing dataset. For testing dataset, low dose measurement was simulated by the same way as training dataset. Throughout all experiments, 5120 pairs were included in training dataset, and 1280 pairs in testing dataset.

B. Training scheme

Two types of training schemes were conducted in this paper.

- *Different models for different dose levels.* In this training scheme, for each dose level, all deep learning methods trained one specific model using the measurements with the same dose level, and also tested it on the measurements with the same dose level. Totally 4 dose levels were evaluated: $I_i = 1 \times 10^5, 5 \times 10^4, 1 \times 10^4, 5 \times 10^3$.
- *One universal model for different dose levels.* In this training scheme, all deep learning methods trained a single model using the measurements with varying dose levels, and also tested on the measurements with varying dose levels. In this case, each measurement in training dataset was generated with its dose level randomly selected from $\{1 \times 10^5, 7.5 \times 10^4, 5 \times 10^4, 2.5 \times 10^4, 1 \times 10^4, 7.5 \times 10^3, 5 \times 10^3\}$, and each measurement in validation/testing dataset was generated by with its dose level $I_i = 1 \times 10^5, 5 \times 10^4, 1 \times 10^4, 5 \times 10^3$ respectively.

C. Comparison Method

The performance of the proposed methods was evaluated in comparison with classic FBP method, TV method, KSVD [54], BM3D [55], FBPCNN [34], MoDL [44], Neumann Network [45], Projected Gradient Descent (PGD) [17]

and Learned Primal-Dual (Learned-PD) [19]. We only brief these methods and more details can be found in Appendix A.

- The TV method is a well-established classic method, which is often solved via the ADMM solver:

$$\mathbf{x}^{k+1} = \arg \min_{\mathbf{x}} \frac{1}{2} \|\mathbf{Ax} - \mathbf{y}\|_2^2 + \frac{\mu}{2} \|\nabla \mathbf{x} - \mathbf{z}^k + \frac{\mathbf{p}^k}{\mu}\|_2^2,$$

$$\mathbf{z}^{k+1} = \arg \min_{\mathbf{z}} \lambda \|\mathbf{z}\|_1 + \frac{\mu}{2} \|\mathbf{z} - (\nabla \mathbf{x}^{k+1} + \frac{\mathbf{p}^k}{\mu})\|_2^2,$$

$$\mathbf{p}^{k+1} = \mathbf{p}^k + \mu(\nabla \mathbf{x}^{k+1} - \mathbf{z}^{k+1}).$$

The parameters λ, μ in the TV method are manually tuned-up for optimal performance under different dose levels.

- FBPCNN [34] is one representative deep-learning-based method for CT reconstruction that use the deep NN as a post-process technique, where an NN with U-net-based CNN is trained to directly denoise the image reconstructed by the FBP method.
- MoDL [44] is a deep learning method proposed for MRI reconstruction, which also can be used for LDCT reconstruction. MoDL unrolls the following iterative scheme

$$\begin{aligned} \mathbf{x}^k &= (\mathbf{A}^T \mathbf{A} + \lambda \mathbf{I})^{-1} (\mathbf{A}^T \mathbf{y} + \lambda \tilde{\mathbf{x}}^{k-1}), \\ \tilde{\mathbf{x}}^k &= \mathcal{D}_{\text{cnn}}(\mathbf{x}^k; \theta^k), \end{aligned}$$

where \mathcal{D}_{cnn} is a CNN-based denoiser and λ is learned as an NN weight.

- Neumann-Net [45] is proposed for linear inverse problem in generic imaging, whose iterative scheme is as follows:

$$\mathbf{x}^K = \sum_{k=0}^{K-1} \mathbf{x}^k + \eta (\mathbf{I} - \eta \mathbf{A}^T \mathbf{A}) \mathbf{x}^{K-1} - \eta \mathcal{D}_{\text{cnn}}(\mathbf{x}^{K-1}; \theta^{K-1}),$$

where \mathcal{D}_{cnn} is a CNN-based mapping and $\mathbf{x}^0 = \mathbf{A}^T \mathbf{y}$.

- PGD [17] is proposed for CT reconstruction with the following iterative scheme:

$$\mathbf{x}^{k+1} = (1 - \alpha_k) \mathbf{x}^k + \alpha_k \mathcal{D}_{\text{cnn}}(\mathbf{x}^k - \gamma (\mathbf{A}^T \mathbf{Ax}^k - \mathbf{A}^T \mathbf{y})),$$

where \mathcal{D}_{cnn} is a CNN-based mapping and α_k and γ are parameters.

- Learned-PD [19] is the unrolling-based method proposed for CT reconstruction. By setting the initial value as \mathbf{x}^0 and introducing the dual variable \mathbf{h}^0 , the iterative scheme based on PDHG algorithm is derived:

$$\mathbf{h}^k = \mathcal{D}_{\text{cnn}}^{\theta_d}(\mathbf{h}^{k-1} + \sigma \mathbf{Ax}^{k-1}, \mathbf{y}),$$

$$\mathbf{x}^k = \mathcal{D}_{\text{cnn}}^{\theta_p}(\mathbf{x}^{k-1} - \tau \mathbf{A}^T \mathbf{h}^{k-1}),$$

$$\tilde{\mathbf{x}}^k = \mathbf{x}^{k-1} + \theta (\mathbf{x}^k - \mathbf{x}^{k-1}),$$

where θ_d and θ_p are the parameters of the dual proximal and the primal proximal respectively, σ and τ are the step lengths, and θ is the overrelaxation parameter.

V. RESULTS

In this section the proposed AHP-Net is evaluated on the simulated prostate CT data.

A. Quantitative comparison on dataset

Three metrics, peak signal to noise ratio (PSNR), root mean square error (RMSE) and structural similarity index measure (SSIM) [56], are used for quantitative evaluation of image quality. Recall that PSNR is defined as

$$\text{PSNR}(\mathbf{x}, \mathbf{x}^*) = -10 \log_{10} \left(\frac{\|\mathbf{x} - \mathbf{x}^*\|_2^2}{\max_i |x_i|^2} \right),$$

where \mathbf{x}^* denotes reconstructed image and \mathbf{x} denotes ground truth, *i.e.* normal dose image.

See Table I for the quantitative comparison of the results from different methods, where different models were trained for processing the data w.r.t. different dose levels. It can be seen that the performance of Neumann-Net is noticeably worse than the other. One possible reason might be that Neumann-Net need more iterations rather than only 3 stages. Three deep learning methods, FBPCovNet, MoDL and PGD, improved the reconstruction results. The proposed AHP-Net and Learned-PD are two best performers among all methods. In the case of relatively high dose level, $I_i = 1 \times 10^5, 5 \times 10^4$, the performances of these two methods are very close. In the case of relatively low dose level, $I_i = 1 \times 10^4, 5 \times 10^3$, the proposed AHP-Net outperformed Learned-PD by a noticeably margin, 1.7 – 2.5 dB advantage in PSNR.

See Table II for the quantitative comparison of the results from different methods, where one single model was trained for processing the data with varying dose levels. Again, Neumann-Net don't perform as well as the others. The proposed AHP-Net is the best performer among all. The performance advantage of the proposed AHP-Net over the second best performer (Learned-PD) is around 1.5 dB for higher dose levels and 2.2 dB for lower dose levels.

Indeed, while the performance of the universal model trained for varying dose levels is compared to that of the individual models trained for each fixed dose level, the proposed AHP-Net see the smallest performance hit, which ranges from 0.3 – 0.6dB in PSNR, in the case of low dose levels. Even so, by comparing Table I and Table II, the universal model of the AHP-Net still outperformed multiple models of other compared methods, in all tested dose levels.

In short, the proposed AHP-Net showed its advantage over existing representative non-learning methods and deep learning methods, specially when the dose level is low. Also, the proposed AHP has its advantage in terms of practical usage, as it allows to train a single model to processing the data w.r.t. varying dose levels with very competitive performance. The outcome of quantitative comparison clearly indicates the importance of the setting of hyper-parameters to optimization-unrolling-based deep learning methods and the effectiveness of our solution to it.

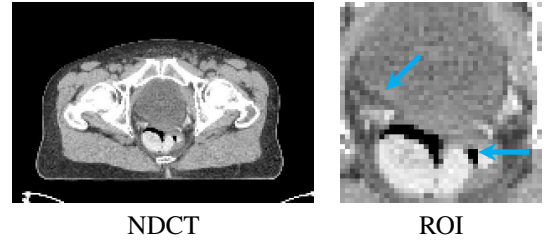


Fig. 4: Normal dose CT image and zoomed region (ROI).

B. Visual comparison of some examples

Due to space limitation, only the images reconstructed by different methods from one sample measurement are shown for visual comparison. The dose level of the measurement is $I_i = 1 \times 10^4$. The displayed window is set to $[-150, 150]$ HU for all figures. More results w.r.t. other dose levels can be found in Appendix B for visual comparison.

Fig. 4 demonstrates the selected normal dose CT (NDCT) image and the zoomed region of interesting (ROI). For the image reconstructed by the non-learning methods and the NN models trained by deep learning methods, specifically for the dose level $I_i = 5 \times 10^3$, Fig. 5 shows the images reconstructed by different methods, and their zoomed-in images of boxes in Fig. 4 are displayed in Fig. 6. As shown by the cyan arrows, in comparison to he zoomed-in NDCT image, the results of FBPCovNet, MoDL, Neumann-Net, PGD and Learned-PD were more blurred than that of the proposed method. See Table III for quantitative comparison of the results shown in Fig. 5.

For the image reconstructed by the non-learning methods and the universal NN model trained by deep learning methods for varying dose levels, specifically for the dose level $I_i = 1 \times 10^4$, Fig. 7 shows the images reconstructed by different methods, and their zoomed-in images of boxes in Fig. 4 are displayed in Fig. 8. As shown by the cyan arrows, in comparison to he zoomed-in NDCT image, the results of FBPCovNet, MoDL, Neumann-Net, PGD and Learned-PD were more blurred than that of the proposed method. See Table III for quantitative comparison for the results shown in Fig. 7.

For the hyper-parameters set in MBIR, Fig. 9 shows the predicted hyper-parameters at different dose levels by the universal models trained for varying dose levels. It can be seen that the predicted hyper-parameter adapts well with inputs of different noise levels, where a lower-dose-level input requires larger hyper-parameter to incorporate more prior knowledge, and vice versa.

C. Ablation study

The ablation study conducted in this section focuses on how the following two parts impact the performance of image reconstruction: (1) the introduction of an MLP for adaptive prediction of the hyper-parameters and (2) the usages of 8 high-pass filters from B-spline framelet. Through the whole ablation study, all different versions of the AHP-Net are trained by the same procedure on the same training/validation dataset and tested on the same testing dataset. Different dose

TABLE I: Quantitative comparison (Mean \pm STD) of the results reconstructed by different methods on testing dataset, where different models are trained for different dose levels in deep learning methods.

Dose level	Index	FBP	TV	KSVD	BM3D	FBPConvNet
1×10^5	PSNR	37.15 \pm 2.04	39.75 \pm 2.18	35.61 \pm 3.46	37.27 \pm 2.15	38.14 \pm 2.02
	RMSE	19.06 \pm 1.10	14.18 \pm 1.38	24.31 \pm 2.34	20.07 \pm 1.35	17.05 \pm 1.48
	SSIM	0.9336 \pm 0.01	0.9685 \pm 0.01	0.9149 \pm 0.02	0.9297 \pm 0.02	0.9788 \pm 0.01
5×10^4	PSNR	35.78 \pm 2.05	38.85 \pm 2.18	34.84 \pm 2.09	34.31 \pm 1.97	38.11 \pm 2.01
	RMSE	22.34 \pm 1.55	15.72 \pm 1.54	25.07 \pm 3.45	21.16 \pm 2.08	17.13 \pm 1.82
	SSIM	0.8963 \pm 0.02	0.9594 \pm 0.01	0.8947 \pm 0.02	0.9165 \pm 0.02	0.9751 \pm 0.01
1×10^4	PSNR	30.23 \pm 2.22	34.21 \pm 2.31	30.37 \pm 2.16	31.46 \pm 2.32	35.42 \pm 2.12
	RMSE	42.60 \pm 5.74	26.97 \pm 4.01	39.58 \pm 5.03	34.91 \pm 4.65	23.35 \pm 2.42
	SSIM	0.6883 \pm 0.06	0.8645 \pm 0.05	0.7351 \pm 0.07	0.8046 \pm 0.06	0.9616 \pm 0.01
5×10^3	PSNR	26.77 \pm 2.32	30.42 \pm 2.43	27.53 \pm 2.47	29.42 \pm 2.07	33.39 \pm 2.01
	RMSE	63.63 \pm 10.38	41.94 \pm 7.83	54.90 \pm 9.67	44.17 \pm 8.74	29.51 \pm 3.19
	SSIM	0.5401 \pm 0.07	0.7178 \pm 0.08	0.6124 \pm 0.09	0.7267 \pm 0.08	0.9453 \pm 0.01
Dose level	Index	NeumannNet	MoDL	PGD	Learned-PD	AHP-Net
1×10^5	PSNR	35.17 \pm 2.14	38.94 \pm 3.33	38.27 \pm 2.03	41.16 \pm 2.12	41.12 \pm 2.69
	RMSE	24.20 \pm 3.87	16.88 \pm 4.58	16.76 \pm 1.12	12.08 \pm 1.39	12.41 \pm 3.31
	SSIM	0.9442 \pm 0.02	0.9842 \pm 0.02	0.9590 \pm 0.01	0.9863 \pm 0.00	0.9875 \pm 0.01
5×10^4	PSNR	34.81 \pm 2.17	38.09 \pm 2.80	38.14 \pm 2.07	39.25 \pm 2.09	39.55 \pm 3.08
	RMSE	25.19 \pm 3.65	17.80 \pm 6.79	17.03 \pm 1.37	15.02 \pm 1.57	14.98 \pm 5.06
	SSIM	0.9354 \pm 0.02	0.9796 \pm 0.01	0.9531 \pm 0.01	0.9808 \pm 0.01	0.9819 \pm 0.01
1×10^4	PSNR	33.27 \pm 2.08	36.20 \pm 2.55	35.53 \pm 2.24	35.69 \pm 2.10	38.20 \pm 2.50
	RMSE	29.98 \pm 3.77	21.65 \pm 5.25	23.10 \pm 2.84	22.64 \pm 2.34	17.26 \pm 4.60
	SSIM	0.8736 \pm 0.03	0.9656 \pm 0.01	0.9602 \pm 0.01	0.9637 \pm 0.01	0.9738 \pm 0.01
5×10^3	PSNR	32.16 \pm 2.07	35.07 \pm 2.81	34.91 \pm 2.15	35.16 \pm 2.14	36.93 \pm 2.42
	RMSE	34.07 \pm 4.05	25.23 \pm 13.45	24.73 \pm 2.26	24.10 \pm 2.74	19.84 \pm 3.95
	SSIM	0.8017 \pm 0.04	0.9605 \pm 0.02	0.9527 \pm 0.01	0.9594 \pm 0.01	0.9673 \pm 0.01

TABLE II: Quantitative comparison (Mean \pm STD) of the results reconstructed by different methods on testing dataset, where one single model is trained for different dose levels in deep learning methods.

Dose level	Index	FBPConvNet	NeumannNet	MoDL	PGD	Learned-PD	AHP-Net
1×10^5	PSNR	37.44 \pm 1.94	35.06 \pm 2.12	34.30 \pm 6.21	38.29 \pm 2.06	39.07 \pm 1.99	40.54 \pm 2.42
	RMSE	18.49 \pm 1.75	24.50 \pm 3.80	35.89 \pm 36.30	16.75 \pm 1.43	15.34 \pm 1.54	13.15 \pm 2.97
	SSIM	0.9718 \pm 0.01	0.9434 \pm 0.02	0.9481 \pm 0.07	0.9776 \pm 0.01	0.9820 \pm 0.00	0.9855 \pm 0.01
5×10^4	PSNR	37.06 \pm 1.96	34.94 \pm 2.12	34.21 \pm 5.83	38.04 \pm 2.07	38.46 \pm 2.02	40.07 \pm 2.40
	RMSE	19.32 \pm 1.77	24.82 \pm 3.77	34.73 \pm 31.78	17.25 \pm 1.48	16.45 \pm 1.64	13.85 \pm 2.96
	SSIM	0.9695 \pm 0.01	0.9366 \pm 0.02	0.9489 \pm 0.06	0.9761 \pm 0.02	0.9792 \pm 0.01	0.9832 \pm 0.01
1×10^4	PSNR	34.76 \pm 2.11	33.82 \pm 2.07	33.21 \pm 4.86	36.15 \pm 2.17	35.88 \pm 2.14	37.92 \pm 2.37
	RMSE	25.19 \pm 2.63	28.17 \pm 3.60	35.67 \pm 26.71	21.48 \pm 2.27	22.16 \pm 2.31	17.65 \pm 3.14
	SSIM	0.9508 \pm 0.01	0.8759 \pm 0.03	0.9447 \pm 0.05	0.9642 \pm 0.01	0.9641 \pm 0.01	0.9713 \pm 0.01
5×10^3	PSNR	32.71 \pm 2.23	32.22 \pm 2.10	32.06 \pm 4.61	33.94 \pm 2.33	34.12 \pm 2.21	36.39 \pm 2.38
	RMSE	32.02 \pm 4.31	33.78 \pm 3.96	39.82 \pm 28.93	27.87 \pm 4.38	27.15 \pm 3.22	21.03 \pm 3.59
	SSIM	0.9230 \pm 0.03	0.7947 \pm 0.04	0.9305 \pm 0.06	0.9425 \pm 0.02	0.9498 \pm 0.01	0.9603 \pm 0.02

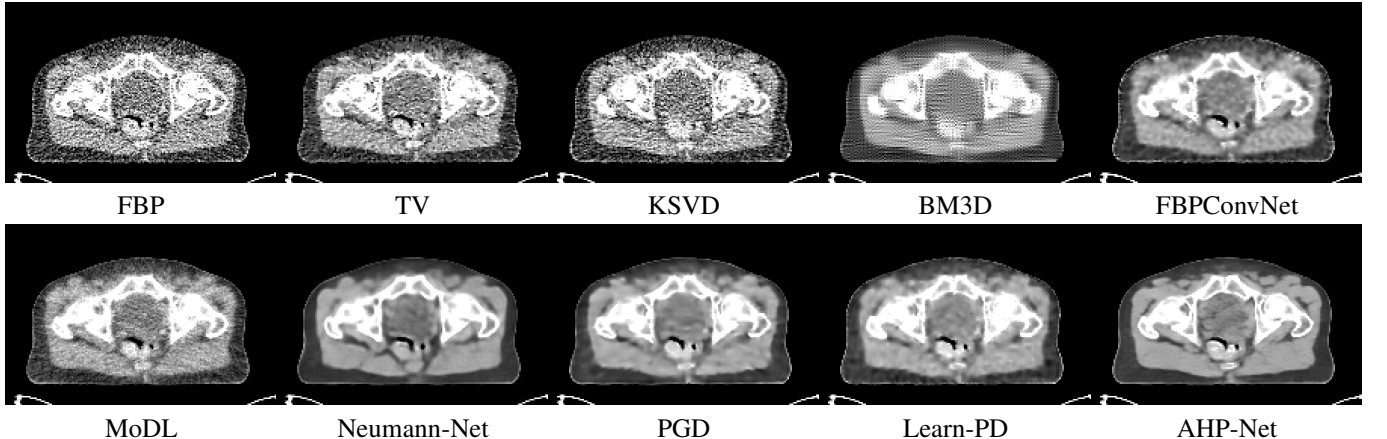


Fig. 5: Reconstruction results at dose level $I_i = 5 \times 10^3$ by the models trained under same dose level.

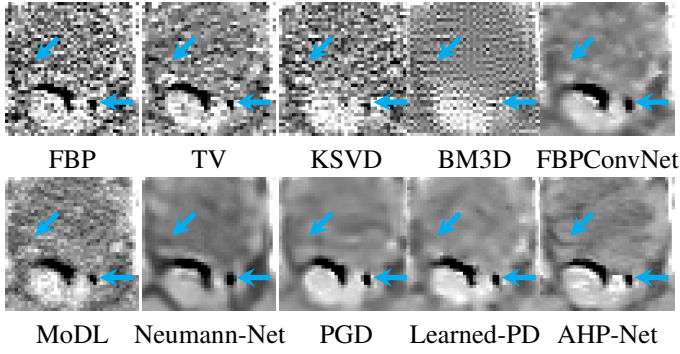


Fig. 6: Zoom-in results of Fig. 5.

TABLE III: Quantitative metrics on the reconstruction results for the image slice shown in Fig. 5 and Fig. 7.

Method	Index	FBP	TV	KSVD	BM3D	FBPCovNet	MoDL	Neumann-Net	PGD	Learned-PD	AHP-Net
Fig. 5	PSNR	25.12	28.09	25.53	27.42	30.07	31.83	28.85	32.03	31.65	33.71
	RMSE	57.78	41.06	54.90	44.17	32.68	26.70	37.60	26.09	27.25	21.49
	SSIM	0.7278	0.8509	0.6124	0.7267	0.9222	0.9377	0.9042	0.9412	0.9425	0.9522
Fig. 7	PSNR	28.31	31.65	28.37	29.46	31.39	31.34	29.50	32.90	32.56	34.89
	RMSE	40.03	27.24	39.58	34.91	28.06	28.22	34.91	23.59	24.55	18.77
	SSIM	0.8430	0.9355	0.7351	0.8046	0.9283	0.9356	0.923	0.9505	0.9504	0.9617

levels are trained with different models. See Table IV for the results from the different versions.

- *no filter vs spline framelet filter bank.* To verify the effectiveness of the spline framelet filter bank of the proposed AHP-Net, the same NN but there is no filter was adopted. We set $z^k = x^k$, which the method is the same as MoDL. See the comparison of the column titled “No Filter” vs “AHP-Net” in Table IV. The results under different dose level showed the advantage of 8 filters over no filter, about 1.5–2.2 dB in PSNR, which indicates the joint benefits of framelet filter bank and adaptive hyper-parameters.
- ∇ vs spline framelet filter bank. The ablation study was performed on AHP-Net and the same NN but whose 8 framelet filters are replaced by 2 filters of ∇ ($[1, -1], [1, -1]^T$) seen in TV regularization. See the comparison of the column titled as “Using ∇ ” vs “AHP-Net” in Table IV. The results under different dose level showed the advantage of 8 filters over gradient operator ∇ , about 1.1–1.9 dB in PSNR. It is noted that in addition to performance gain by using the framelet filter bank, the performance benefit brought by MLP-based predictor is also fully exploited when using ∇ , as only 2 parameters are involved when using ∇ .
- *Learnable filters vs Spline framelet filter bank.* It would be interesting to see whether a learnable filter outperformed our spline frame filter; see the column titled as “Learnable filters” in Table IV. In the case of $I_i = 1 \times 10^5$, the performance gain of learning an MLP for adaptive prediction of hyper-parameters is 0.5dB in PSNR. In the case of lower dose levels, $I_i = 5 \times 10^4, 1 \times 10^4, 5 \times 10^3$, there is a significant improvement of the proposed method over “Learnable filters”, about 1.3–1.7dB in PSNR. One possible cause is that network training needs to solve a highly non-

TABLE IV: Quantitative comparison (Mean \pm STD) of the results reconstructed by the different versions of the AHP-Net for ablation study

Dose level	Index	No Filter	Using ∇	Learnable filters	Learnable HP	AHP-Net
1×10^5	PSNR	38.94 \pm 3.33	39.26 \pm 2.86	39.62 \pm 2.50	40.86 \pm 2.54	41.12 \pm 2.69
	RMSE	16.88 \pm 14.58	15.46 \pm 4.62	14.67 \pm 3.66	12.80 \pm 4.10	12.41 \pm 3.31
	SSIM	0.9841 \pm 0.02	0.9656 \pm 0.01	0.9856 \pm 0.01	0.9686 \pm 0.02	0.9875 \pm 0.01
5×10^4	PSNR	38.09 \pm 2.80	38.41 \pm 2.98	38.27 \pm 2.50	39.03 \pm 3.11	39.55 \pm 3.08
	RMSE	17.80 \pm 6.79	17.25 \pm 7.16	17.13 \pm 4.43	16.14 \pm 7.24	14.98 \pm 5.06
	SSIM	0.9796 \pm 0.01	0.9566 \pm 0.02	0.9812 \pm 0.01	0.9618 \pm 0.02	0.9819 \pm 0.01
1×10^4	PSNR	36.20 \pm 2.55	36.91 \pm 2.49	36.46 \pm 2.49	36.78 \pm 2.42	38.20 \pm 2.50
	RMSE	21.65 \pm 5.21	19.98 \pm 4.51	20.97 \pm 4.09	20.14 \pm 3.59	17.26 \pm 4.60
	SSIM	0.9656 \pm 0.01	0.9383 \pm 0.02	0.9712 \pm 0.01	0.9368 \pm 0.02	0.9738 \pm 0.01
5×10^3	PSNR	35.07 \pm 2.81	35.08 \pm 3.31	35.31 \pm 2.45	35.63 \pm 2.49	36.85 \pm 1.85
	RMSE	25.23 \pm 13.45	26.21 \pm 19.65	23.88 \pm 4.45	23.08 \pm 5.19	36.93 \pm 2.42
	SSIM	0.9605 \pm 0.02	0.9191 \pm 0.05	0.9624 \pm 0.01	0.9229 \pm 0.03	0.9673 \pm 0.01

convex optimization problem with millions of network parameters. The filter bank plays an important role in the performance of the NN. However, when they are treated as one part of network parameters, they do not receive sufficient attention in the training.

- *Learning constant hyper-parameters as network weights vs Using an MLP for adaptive prediction of hyper-parameters.* The results from the proposed AHP-Net are compared to that from the same NN but whose hyper-parameters $\{\beta_j^k\}$ are treated as network parameters learned on training dataset; see the column titled as “Learnable HP” in Table IV. In the case of higher dose levels, $I_i = 1 \times 10^5, 5 \times 10^4$, the performance gain of learning an MLP for adaptive prediction of hyper-parameters is about 0.3–0.5 dB in PSNR. In the case of lower dose levels, $I_i = 1 \times 10^4, 5 \times 10^3$, there is a significant improvement of MLP-based adaptive prediction over learnable constant hyper-parameters, about 1.2–1.4 dB in PSNR.

Fig. 10 visualized a comparison result from different versions of the AHP-Net with dose level $I_i = 5 \times 10^4$, and Fig. 11 shows their zoomed-in regions of the boxes in Fig. 4. It can be seen that these figures correspond well with the results shown in Table IV; see more comparison in supplementary file.

D. Cross-validation

In this section, a k -fold cross-validation is conducted on FBPCovNet and the proposed AHP-Net to give a comprehensive measure of its model’s performance throughout the whole dataset. More specifically, 100 scans are equally partitioned into 5 folders. Then, for each folder, the images associated with the scans from this fold are used for testing, and all others are used for training. One single model is trained for different noise levels. See Table V for the list of average quantitative metric values of the results from each test dataset. The mean of PSNR for the results from the proposed AHP-Net is about 2.4–3.5dB higher than that of FBPCovNet. However, the difference of the STD of PSNR is no more than 0.25dB.

VI. DISCUSSION AND CONCLUSION

Similarly to many optimization-unrolling-based deep learning methods, this paper also proposed a deep learning method for LDCT image reconstruction, the AHP-Net, that unrolls

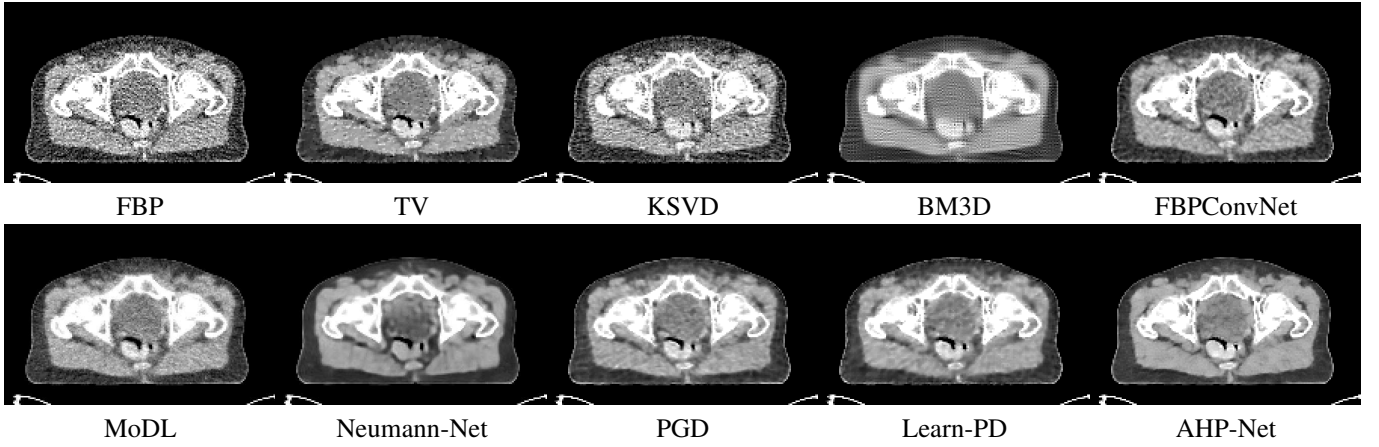


Fig. 7: Reconstruction results at dose level $I_i = 1 \times 10^4$ by the universal models trained for varying dose levels.

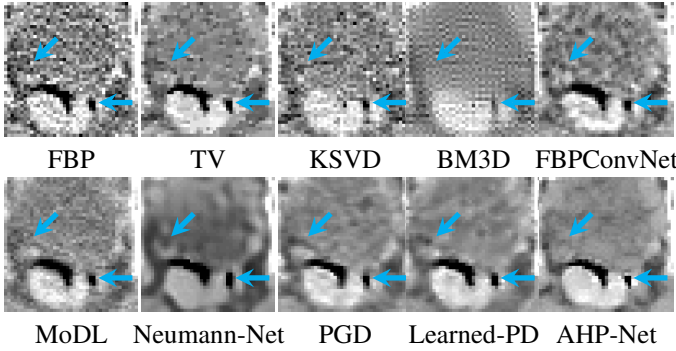


Fig. 8: Zoom-in results of Fig. 7.

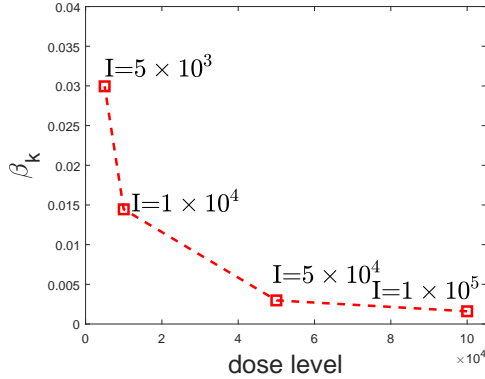


Fig. 9: Predicted hyper-parameter at different dose levels by the universal models trained for varying dose levels.

the half-quadratic splitting scheme for MBIR. Each stage of the AHP-Net contains one inversion block and a denoising block, where the denoising block is built-on a CNN. The main difference of the proposed AHP-Net from other deep learning solutions lies the design of the inversion block.

In the proposed inversion block, we replaced the often-used gradient operator ∇ by the filter banks with 8 high-pass filters from linear spline framelet transform, motivated by its success in ℓ_1 -norm relating regularization in image recovery.

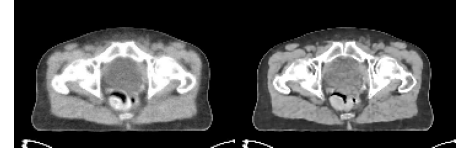


Fig. 10: Reconstruction results at dose level $I_i = 5 \times 10^4$ by the models trained under same dose level. (a) No filter; (b) Using ∇ ; (c) Learnable filters; (d) Learnable HP; (e) AHP-net.

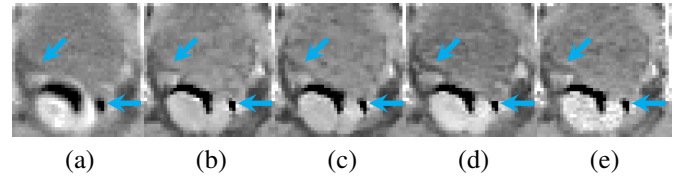


Fig. 11: Zoom-in results of Fig. 10 corresponding to the red boxes in Fig. 4. (a) No Filter; (b) Using ∇ ; (c) Learnable filters; (d) Learnable HP; (e) AHP-net.

Moreover, we proposed to pay special attention to the hyper-parameters involved in the inversion block, and presented a MLP-based NN to predict hyper-parameters that adaptive to both dose level and image content.

The experiments showed the advantage of the proposed method over classic non-learning methods and some representative deep learning based methods for LDCT reconstruction. Also, another advantage is that the proposed method can only train a single model with competitive performance to process measurement data with varying dose levels.

As different dose levels implicitly refers to different SNRs. The proposed methods indeed allows to train a universal model with competitive performance to process the data with un-

TABLE V: Cross-validation Quantitative results of one single model trained for different dose levels.

Dose level	Method	Index	Fold 1	Fold 2	Fold 3	Fold 4	Fold 5	Mean±STD
1×10^5	FBPConvNet	PSNR	37.81	37.69	38.15	37.06	37.44	37.63 ± 0.41
		RMSE	17.24	17.03	16.36	18.33	18.49	17.49 ± 0.90
		SSIM	0.9741	0.9746	0.9755	0.9736	0.9855	0.9739 ± 0.00
	AHP-Net	PSNR	39.68	40.24	39.40	40.06	40.54	39.98 ± 0.45
		RMSE	15.57	13.24	14.43	13.19	13.15	13.92 ± 1.07
		SSIM	0.9834	0.9778	0.9821	0.9769	0.9703	0.9811 ± 0.01
5×10^4	FBPConvNet	PSNR	37.26	37.20	37.46	36.73	37.06	37.14 ± 0.27
		RMSE	18.35	18.00	17.69	19.04	19.32	18.48 ± 0.69
		SSIM	0.9717	0.9723	0.9724	0.9718	0.9695	0.9715 ± 0.00
	AHP-Net	PSNR	39.30	38.29	39.02	39.72	40.07	39.58 ± 0.42
		RMSE	16.15	13.87	15.02	13.69	13.85	14.52 ± 1.06
		SSIM	0.9811	0.9757	0.9800	0.9748	0.9832	0.9790 ± 0.00
1×10^4	FBPConvNet	PSNR	34.63	34.68	34.69	34.53	34.76	34.66 ± 0.09
		RMSE	24.83	24.10	24.36	24.58	25.19	24.61 ± 0.42
		SSIM	0.9562	0.9548	0.9566	0.9552	0.9508	0.9547 ± 0.01
	AHP-Net	PSNR	37.31	37.59	37.21	37.95	37.92	37.59 ± 0.34
		RMSE	19.72	17.60	18.38	16.70	17.65	18.01 ± 1.13
		SSIM	0.9684	0.9634	0.9685	0.9634	0.9713	0.9670 ± 0.00
5×10^3	FBPConvNet	PSNR	32.60	32.68	32.78	32.30	32.71	32.61 ± 0.19
		RMSE	31.39	30.42	30.40	31.91	32.02	31.23 ± 0.78
		SSIM	0.9355	0.9310	0.9375	0.9266	0.9230	0.9307 ± 0.01
	AHP-Net	PSNR	35.72	36.03	35.87	36.57	36.39	36.12 ± 0.36
		RMSE	23.57	20.97	21.40	19.54	21.03	21.30 ± 1.45
		SSIM	0.9563	0.9522	0.9587	0.9536	0.9603	0.9562 ± 0.00

known SNRs, which can be valuable to practical applications in medical CT imaging. In practical medical CT scans, the dose level is not fixed and the SNR of the data is also different for different people under the same dose level, *e.g.* adult vs child. The adaptivity of the proposed method to different SNRs of data can be welcomed in practice.

There still exists some issues in the proposed method. One is that instead of reconstructing the 3D volume as a whole, the proposed method separately reconstructs image slices. The main reason we take such a reconstruction scheme is that the number of network parameters of the NN adopted in this paper will increase exponentially when constructing the whole 3D volume. The resulting memory usage in GPU will be too excessive to make the computation feasible under current available commodity GPUs.

In future work, we will study how to design compact deep NN that can directly reconstruct 3D volume in LDCT image reconstruction. Also, we will investigate the applications of the proposed method in other medical image reconstruction problems, *e.g.* sparse-view CT reconstruction and image reconstruction from sparse samples in MRI.

REFERENCES

- [1] E. Y. Sidky, C.-M. Kao, and X. Pan, "Accurate image reconstruction from few-views and limited-angle data in divergent-beam CT," *Journal of X-ray Science and Technology*, vol. 14, no. 2, pp. 119–139, 2006.
- [2] B. R. Whiting, P. Massoumzadeh, O. A. Earl, J. A. O Sullivan, D. L. Snyder, and J. F. Williamson, "Properties of preprocessed sinogram data in X-ray computed tomography," *Medical physics*, vol. 33, no. 9, pp. 3290–3303, 2006.
- [3] J.-B. Thibault, K. D. Sauer, C. A. Bouman, and J. Hsieh, "A three-dimensional statistical approach to improved image quality for multislice helical CT," *Medical physics*, vol. 34, no. 11, pp. 4526–4544, 2007.
- [4] J. Nuyts, B. De Man, J. A. Fessler, W. Zbijewski, and F. J. Beekman, "Modelling the physics in the iterative reconstruction for transmission computed tomography," *Physics in medicine and biology*, vol. 58, no. 12, p. R63, 2013.
- [5] X. Zhang and J. Froment, "Total variation based fourier reconstruction and regularization for computer tomography," in *Nuclear Science Symposium Conference Record, 2005 IEEE*, vol. 4, pp. 2332–2336, IEEE, 2005.
- [6] E. Y. Sidky and X. Pan, "Image reconstruction in circular cone-beam computed tomography by constrained, total-variation minimization," *Physics in Medicine & Biology*, vol. 53, no. 17, p. 4777, 2008.

- [7] G. Chen, J. Tang, and S. Leng, "Prior image constrained compressed sensing (PICCS): a method to accurately reconstruct dynamic CT images from highly undersampled projection data sets," *Medical physics*, vol. 35, no. 2, pp. 660–663, 2008.
- [8] X. Jia, B. Dong, Y. Lou, and S. B. Jiang, "GPU-based iterative cone-beam CT reconstruction using tight frame regularization," *Physics in Medicine & Biology*, vol. 56, no. 13, p. 3787, 2011.
- [9] H. Gao, R. Li, Y. Lin, and L. Xing, "4D cone beam CT via spatiotemporal tensor framelet," *Medical physics*, vol. 39, no. 11, pp. 6943–6946, 2012.
- [10] X. Jia, Y. Lou, B. Dong, Z. Tian, and S. Jiang, "4D computed tomography reconstruction from few-projection data via temporal non-local regularization," in *International Conference on Medical Image Computing and Computer-Assisted Intervention*, pp. 143–150, Springer, 2010.
- [11] H. Gao, J. Cai, Z. Shen, and H. Zhao, "Robust principal component analysis-based four-dimensional computed tomography," *Physics in Medicine & Biology*, vol. 56, no. 11, p. 3181, 2011.
- [12] H. Gao, H. Yu, S. Osher, and G. Wang, "Multi-energy CT based on a prior rank, intensity and sparsity model (PRISM)," *Inverse problems*, vol. 27, no. 11, p. 115012, 2011.
- [13] J. Cai, X. Jia, H. Gao, S. B. Jiang, Z. Shen, and H. Zhao, "Cine cone beam CT reconstruction using low-rank matrix factorization: algorithm and a proof-of-principle study," *IEEE transactions on medical imaging*, vol. 33, no. 8, pp. 1581–1591, 2014.
- [14] G. Chen and Y. Li, "Synchronized multiartifact reduction with tomographic reconstruction (SMART-RECON): A statistical model based iterative image reconstruction method to eliminate limited-view artifacts and to mitigate the temporal-average artifacts in time-resolved CT," *Medical physics*, vol. 42, no. 8, pp. 4698–4707, 2015.
- [15] Q. Xu, H. Yu, X. Mou, L. Zhang, J. Hsieh, and G. Wang, "Low-dose X-ray CT reconstruction via dictionary learning," *IEEE transactions on medical imaging*, vol. 31, no. 9, pp. 1682–1697, 2012.
- [16] T. Bai, H. Yan, X. Jia, S. Jiang, G. Wang, and X. Mou, "Z-index parameterization for volumetric CT image reconstruction via 3-D dictionary learning," *IEEE transactions on medical imaging*, vol. 36, no. 12, pp. 2466–2478, 2017.
- [17] H. Gupta, K. H. Jin, H. Q. Nguyen, M. T. McCann, and M. Unser, "CNN-based projected gradient descent for consistent CT image reconstruction," *IEEE transactions on medical imaging*, vol. 37, no. 6, pp. 1440–1453, 2018.
- [18] J. He, Y. Yang, Y. Wang, D. Zeng, Z. Bian, H. Zhang, J. Sun, Z. Xu, and J. Ma, "Optimizing a parameterized plug-and-play ADMM for iterative low-dose CT reconstruction," *IEEE transactions on medical imaging*, vol. 38, no. 2, pp. 371–382, 2018.
- [19] J. Adler and O. Öktem, "Learned primal-dual reconstruction," *IEEE transactions on medical imaging*, vol. 37, no. 6, pp. 1322–1332, 2018.
- [20] S. Ramani, Z. Liu, J. Rosen, J.-F. Nielsen, and J. A. Fessler, "Regularization parameter selection for nonlinear iterative image restoration and MRI reconstruction using GCV and SURE-based methods," *IEEE Transactions on Image Processing*, vol. 21, no. 8, pp. 3659–3672, 2012.
- [21] P. C. Hansen, "Analysis of discrete ill-posed problems by means of the L-curve," *SIAM review*, vol. 34, no. 4, pp. 561–580, 1992.
- [22] A. R. Conn, N. I. Gould, and P. Toint, "A globally convergent augmented lagrangian algorithm for optimization with general constraints and simple bounds," *SIAM Journal on Numerical Analysis*, vol. 28, no. 2, pp. 545–572, 1991.
- [23] B. Jin, Y. Zhao, and J. Zou, "Iterative parameter choice by discrepancy principle," *IMA Journal of Numerical Analysis*, vol. 32, no. 4, pp. 1714–1732, 2012.
- [24] G. H. Golub, M. Heath, and G. Wahba, "Generalized cross-validation as a method for choosing a good ridge parameter," *Technometrics*, vol. 21, no. 2, pp. 215–223, 1979.
- [25] Y. Wang, W. Yin, and J. Zeng, "Global convergence of ADMM in nonconvex nonsmooth optimization," *Journal of Scientific Computing*, vol. 78, no. 1, pp. 29–63, 2019.
- [26] M. Mardani, H. Monajemi, V. Pappayan, S. Vasanawala, D. Donoho, and J. Pauly, "Recurrent generative adversarial networks for proximal learning and automated compressive image recovery," *arXiv preprint arXiv:1711.10046*, 2017.
- [27] J. Sun, H. Li, Z. Xu, *et al.*, "Deep ADMM-Net for compressive sensing MRI," in *Advances in neural information processing systems*, pp. 10–18, 2016.
- [28] D. Wu, K. Kim, G. El Fakhri, and Q. Li, "Iterative low-dose CT reconstruction with priors trained by artificial neural network," *IEEE transactions on medical imaging*, vol. 36, no. 12, pp. 2479–2486, 2017.

- [29] D. Geman and C. Yang, "Nonlinear image recovery with half-quadratic regularization," *IEEE transactions on Image Processing*, vol. 4, no. 7, pp. 932–946, 1995.
- [30] H. Chen, Y. Zhang, W. Zhang, P. Liao, K. Li, J. Zhou, and G. Wang, "Low-dose CT via convolutional neural network," *Biomedical optics express*, vol. 8, no. 2, pp. 679–694, 2017.
- [31] H. Chen, Y. Zhang, M. K. Kalra, F. Lin, Y. Chen, P. Liao, J. Zhou, and G. Wang, "Low-dose CT with a residual encoder-decoder convolutional neural network," *IEEE transactions on medical imaging*, vol. 36, no. 12, pp. 2524–2535, 2017.
- [32] Y. S. Han, J. Yoo, and J. C. Ye, "Deep residual learning for compressed sensing CT reconstruction via persistent homology analysis," *arXiv preprint arXiv:1611.06391*, 2016.
- [33] H. Li and K. Mueller, "Low-dose CT streak artifacts removal using deep residual neural network," in *Proc. Fully Three-Dimensional Image Reconstruction Radiol. Nucl. Med.(Fully3D)*, pp. 191–194, 2017.
- [34] K. H. Jin, M. T. McCann, E. Froustey, and M. Unser, "Deep convolutional neural network for inverse problems in imaging," *IEEE Transactions on Image Processing*, vol. 26, no. 9, pp. 4509–4522, 2017.
- [35] J. M. Wolterink, T. Leiner, M. A. Viergever, and I. Išgum, "Generative adversarial networks for noise reduction in low-dose CT," *IEEE transactions on medical imaging*, vol. 36, no. 12, pp. 2536–2545, 2017.
- [36] Q. Yang, P. Yan, Y. Zhang, H. Yu, Y. Shi, X. Mou, M. K. Kalra, Y. Zhang, L. Sun, and G. Wang, "Low-dose CT image denoising using a generative adversarial network with wasserstein distance and perceptual loss," *IEEE transactions on medical imaging*, vol. 37, no. 6, pp. 1348–1357, 2018.
- [37] J. C. Ye, Y. Han, and E. Cha, "Deep convolutional framelets: A general deep learning framework for inverse problems," *SIAM Journal on Imaging Sciences*, vol. 11, no. 2, pp. 991–1048, 2018.
- [38] E. Kang, J. Min, and J. C. Ye, "A deep convolutional neural network using directional wavelets for low-dose X-ray CT reconstruction," *Medical physics*, vol. 44, no. 10, pp. e360–e375, 2017.
- [39] E. Kang, J. C. Ye, *et al.*, "Wavelet domain residual network (WavResNet) for low-dose X-ray CT reconstruction," *arXiv preprint arXiv:1703.01383*, 2017.
- [40] H. Chen, Y. Zhang, Y. Chen, J. Zhang, W. Zhang, H. Sun, Y. Lv, P. Liao, J. Zhou, and G. Wang, "LEARN: Learned experts' assessment-based reconstruction network for sparse-data CT," *IEEE transactions on medical imaging*, vol. 37, no. 6, pp. 1333–1347, 2018.
- [41] D. M. Pelt and K. J. Batenburg, "Fast tomographic reconstruction from limited data using artificial neural networks," *IEEE Transactions on Image Processing*, vol. 22, no. 12, pp. 5238–5251, 2013.
- [42] A. Hauptmann, F. Lucka, M. Betcke, N. Huynh, J. Adler, B. Cox, P. Beard, S. Ourselin, and S. Arridge, "Model-based learning for accelerated, limited-view 3-D photoacoustic tomography," *IEEE transactions on medical imaging*, vol. 37, no. 6, pp. 1382–1393, 2018.
- [43] S. Bazrafkan, V. Van Nieuwenhove, J. Soons, J. De Beenhouwer, and J. Sijbers, "Deep neural network assisted iterative reconstruction method for low dose CT," *arXiv preprint arXiv:1906.00650*, 2019.
- [44] H. K. Aggarwal, M. P. Mani, and M. Jacob, "MoDL: Model-based deep learning architecture for inverse problems," *IEEE transactions on medical imaging*, vol. 38, no. 2, pp. 394–405, 2018.
- [45] D. Gilton, G. Ongie, and R. Willett, "Neumann networks for inverse problems in imaging," *arXiv preprint arXiv:1901.03707*, 2019.
- [46] Q. Ding, Y. Long, X. Zhang, and J. A. Fessler, "Statistical Image Reconstruction Using Mixed Poisson-Gaussian Noise Model for X-Ray CT," *arXiv preprint arXiv:1801.09533*, 2018.
- [47] L. Fu, T. Lee, S. M. Kim, A. M. Alessio, P. E. Kinahan, Z. Chang, K. D. Sauer, M. K. Kalra, and B. De Man, "Comparison Between Pre-Log and Post-Log Statistical Models in Ultra-Low-Dose CT Reconstruction," *IEEE Transactions on Medical Imaging*, vol. 36, no. 3, pp. 707–720, 2017.
- [48] K. D. Sauer and C. A. Bouman, "A local update strategy for iterative reconstruction from projections," *IEEE Transactions on Signal Processing*, vol. 41, no. 2, pp. 534–548, 1993.
- [49] J. A. Fessler, "Statistical image reconstruction methods for transmission tomography," *Handbook of medical imaging*, vol. 2, pp. 1–70, 2000.
- [50] B. Dong, Z. Shen, *et al.*, "MRA based wavelet frames and applications," *IAS Lecture Notes Series, Summer Program on "The Mathematics of Image Processing"*, Park City Mathematics Institute, vol. 19, 2010.
- [51] X. Zheng, I. Y. Chun, Z. Li, Y. Long, and J. A. Fessler, "Sparse-View X-Ray CT Reconstruction Using ℓ_1 Prior with Learned Transform," *arXiv preprint arXiv:1711.00905*, 2017.
- [52] G. Huang, Z. Liu, L. Van Der Maaten, and K. Q. Weinberger, "Densely connected convolutional networks," in *Proceedings of the IEEE conference on computer vision and pattern recognition*, pp. 4700–4708, 2017.
- [53] A. Paszke, S. Gross, S. Chintala, G. Chanan, E. Yang, Z. DeVito, Z. Lin, A. Desmaison, L. Antiga, and A. Lerer, "Automatic differentiation in pytorch," 2017.
- [54] Q. Zhang and B. Li, "Discriminative k-svd for dictionary learning in face recognition," in *2010 IEEE computer society conference on computer vision and pattern recognition*, pp. 2691–2698, IEEE, 2010.
- [55] K. Dabov, A. Foi, V. Katkovnik, and K. Egiazarian, "Image denoising by sparse 3-d transform-domain collaborative filtering," *IEEE Transactions on image processing*, vol. 16, no. 8, pp. 2080–2095, 2007.
- [56] Z. Wang, A. C. Bovik, H. R. Sheikh, E. P. Simoncelli, *et al.*, "Image quality assessment: from error visibility to structural similarity," *IEEE transactions on image processing*, vol. 13, no. 4, pp. 600–612, 2004.

APPENDIX

- The details of calculating the gradients of the loss function w.r.t. all parameters, using back-propagation over the deep architecture in Fig. 3.
- The details of the implementation and training of comparison methods
- Visual comparison on more examples.

During the train process, we need to calculate gradients about $\Theta_k = \{\theta_D^{k-1}, \theta_P^k\}$, $k = 1, \dots, K$. The loss of the proposed neural network is as follows,

$$\mathcal{L}(\Theta) = \frac{1}{J} \sum_{j=1}^J \left(\|\mathbf{x}_j^K - \mathbf{x}_j\|_2^2 + \sum_{k=1}^{K-1} \mu_k \|\mathbf{x}_j^k - \mathbf{x}_j\|_2^2 \right), \quad (25)$$

We give the details of the gradient calculation procedure. Recall that the iteration of the proposed method is as follows

$$\tilde{\mathbf{x}}^{k-1} = \mathcal{D}_{\text{cnn}}^{k-1}(\cdot, \theta_P^{k-1}) \quad (26a)$$

$$\beta^k = \mathcal{P}_{\text{mlp}}^k(\cdot, \theta_P^k) \quad (26b)$$

$$\mathbf{z}_i^k = \mathbf{F}_i \tilde{\mathbf{x}}^{k-1} \quad (26c)$$

$$\mathbf{x}^k = \left(\mathbf{A}^\top \mathbf{A} + \sum_{i=1}^L \beta_i^k \mathbf{F}_i^\top \mathbf{F}_i \right)^{-1} \left(\mathbf{A}^\top \mathbf{y} + \sum_{i=1}^L \beta_i^k \mathbf{F}_i^\top \mathbf{z}_i^k \right), \quad (26d)$$

For simplify, we omit the data index j ,

$$\frac{\partial \mathcal{L}(\Theta)}{\partial \theta_P^k} = \frac{\partial \mathcal{L}(\Theta)}{\partial \mathbf{x}^k} \cdot \frac{\partial \mathbf{x}^k}{\partial \theta_P^k}, \quad (27)$$

$$\frac{\partial \mathcal{L}(\Theta)}{\partial \theta_D^{k-1}} = \frac{\partial \mathcal{L}(\Theta)}{\partial \mathbf{x}^k} \cdot \frac{\partial \mathbf{x}^k}{\partial \theta_D^{k-1}}, \quad (28)$$

where

$$\begin{aligned} \frac{\partial \mathcal{L}(\Theta)}{\partial \mathbf{x}^k} &= \mu_k \frac{\partial \|\mathbf{x}^k - \mathbf{x}\|_2^2}{\partial \mathbf{x}^k} + \mu_{k+1} \frac{\partial \|\mathbf{x}^{k+1} - \mathbf{x}\|_2^2}{\partial \mathbf{x}^{k+1}} \cdot \frac{\partial \mathbf{x}^{k+1}}{\partial \mathbf{x}^k} \\ &+ \dots + \mu_{K-1} \frac{\partial \|\mathbf{x}^{K-1} - \mathbf{x}\|_2^2}{\partial \mathbf{x}^{K-1}} \dots \frac{\partial \mathbf{x}^{K-1}}{\partial \mathbf{x}^{K-2}} \cdot \frac{\partial \mathbf{x}^{K-1}}{\partial \mathbf{x}^k}, \\ &+ \frac{\partial \|\mathbf{x}^K - \mathbf{x}\|_2^2}{\partial \mathbf{x}^K} \cdot \frac{\partial \mathbf{x}^K}{\partial \mathbf{x}^{K-1}} \dots \frac{\partial \mathbf{x}^{K-1}}{\partial \mathbf{x}^k}, \end{aligned} \quad (29)$$

and

$$\left\{ \begin{aligned} \frac{\partial \|\mathbf{x}^k - \mathbf{x}\|_2^2}{\partial \mathbf{x}^k} &= 2(\mathbf{x}^k - \mathbf{x}) \end{aligned} \right. \quad (30a)$$

$$\left\{ \begin{aligned} \frac{\partial \mathbf{x}^k}{\partial \mathbf{x}^{k-1}} &= \sum_{i=1}^L \frac{\partial \mathbf{x}^k}{\partial \mathbf{z}_i^k} \frac{\partial \mathbf{z}_i^k}{\partial \tilde{\mathbf{x}}^{k-1}} \frac{\partial \tilde{\mathbf{x}}^{k-1}}{\partial \mathbf{x}^{k-1}}, \end{aligned} \right. \quad (30b)$$

$$\left\{ \begin{aligned} \frac{\partial \mathbf{x}^k}{\partial \theta_D^{k-1}} &= \sum_{i=1}^L \frac{\partial \mathbf{x}^k}{\partial \mathbf{z}_i^k} \frac{\partial \mathbf{z}_i^k}{\partial \tilde{\mathbf{x}}^{k-1}} \frac{\partial \tilde{\mathbf{x}}^{k-1}}{\partial \theta_D^{k-1}}, \end{aligned} \right. \quad (30c)$$

$$\left\{ \begin{aligned} \frac{\partial \mathbf{x}^k}{\partial \theta_P^k} &= \frac{\partial \mathbf{x}^k}{\partial \beta^k} \frac{\partial \beta^k}{\partial \theta_P^k} \end{aligned} \right. \quad (30d)$$

$$\left\{ \begin{aligned} \frac{\partial \mathbf{x}^k}{\partial \mathbf{z}_i^k} &= \beta_i^k \mathbf{F}_i (\mathbf{A}^\top \mathbf{A} + \sum_{i=1}^L \beta_i^k \mathbf{F}_i^\top \mathbf{F}_i)^{-1} \end{aligned} \right. \quad (31a)$$

$$\left\{ \begin{aligned} \frac{\partial \mathbf{x}^k}{\partial \beta_i^k} &= (\mathbf{F}_i^\top \mathbf{z}_i^k - \mathbf{F}_i^\top \mathbf{F}_i \mathbf{x}^k)^T (\mathbf{A}^\top \mathbf{A} + \sum_{i=1}^L \beta_i^k \mathbf{F}_i^\top \mathbf{F}_i)^{-1} \end{aligned} \right. \quad (31b)$$

$$\left\{ \begin{aligned} \frac{\partial \mathbf{z}_i^k}{\partial \tilde{\mathbf{x}}^{k-1}} &= \mathbf{F}_i^T. \end{aligned} \right. \quad (31c)$$

$$\left\{ \begin{aligned} \frac{\partial \beta^k}{\partial \theta_P^k} &= \frac{\mathcal{P}_{\text{fcn}}^k(\mathbf{d}^k, \theta_P^k)}{\partial \theta_P^k}. \end{aligned} \right. \quad (31d)$$

$$\left\{ \begin{aligned} \frac{\partial \tilde{\mathbf{x}}^{k-1}}{\partial \theta_D^k} &= \frac{\mathcal{D}_{\text{cnn}}^k([\mathbf{x}^0, \mathbf{x}^1, \dots, \mathbf{x}^k], \theta_D^k)}{\partial \theta_D^k}, \end{aligned} \right. \quad (31e)$$

A. Comparison Method

1) *PWLS-TV*: The regularization parameter λ is set to 0.01 for $I_i = 1 \times 10^5, 5 \times 10^4$; 0.02 for $I_i = 1 \times 10^4$; and 0.03 for $I_i = 5 \times 10^3$. The parameter μ is set to 10.

2) *MoDL*: was proposed in [44] for MRI reconstruction. We applied it in CT. The details of unrolling stage of MoDL is as follows.

$$\begin{aligned} \mathbf{x}^k &= (\mathbf{A}^\top \mathbf{A} + \lambda \mathbf{I})^{-1} (\mathbf{A}^\top \mathbf{y} + \lambda \tilde{\mathbf{x}}^{k-1}), \\ \tilde{\mathbf{x}}^k &= \mathcal{D}_{\text{cnn}}(\mathbf{x}^k; \theta^k) \end{aligned}$$

where \mathcal{D}_{cnn} is the same neural network as AHP-Net and λ is set as learnable parameter. The loss of MoDL is

$$\mathcal{L}(\Theta) = \frac{1}{J} \sum_{j=1}^J \left(\|\mathbf{x}_j^K - \mathbf{x}_j\|_2^2 + \sum_{k=1}^{K-1} \mu_k \|\mathbf{x}_j^k - \mathbf{x}_j\|_2^2 \right), \quad (32)$$

where $\Theta = (\theta^1, \dots, \theta^K, \lambda)$. For consistency, we set $K = 3$. Adam optimizer was used with the momentum parameter $\beta = 0.9$, mini-batch size to be 4, and the learning rate to be 10^{-4} . The model was trained for 50 epochs.

3) *Neumann-Net*: Neumann Network was proposed in [45] for linear inverse problem in imaging. With step size $\eta > 0$, the inverse problem can be solved by

$$\mathbf{x}^k = \eta \sum_{k=0}^K (\mathbf{I} - \eta \mathbf{A}^\top \mathbf{A} - \eta \mathbf{R})^k \mathbf{A}^\top \mathbf{y}.$$

The details of unrolling stage of Neumann-Net is as follows.

$$\mathbf{x}^k = \sum_{i=0}^{k-1} \mathbf{x}^{i-1} + \eta (\mathbf{I} - \eta \mathbf{A}^\top \mathbf{A}) \mathbf{x}^{k-1} - \eta \mathcal{D}_{\text{cnn}}(\mathbf{x}^{k-1}, \theta^k).$$

The loss of Neumann-Net is

$$\mathcal{L}(\Theta) = \frac{1}{J} \sum_{j=1}^J \left(\|\mathbf{x}_j^K - \mathbf{x}_j\|_2^2 + \sum_{k=1}^{K-1} \mu_k \|\mathbf{x}_j^k - \mathbf{x}_j\|_2^2 \right), \quad (33)$$

where $\Theta = (\theta^1, \dots, \theta^K, \eta)$. For consistency, we set $K = 3$. Adam optimizer was used with the momentum parameter $\beta = 0.9$, mini-batch size to be 4, and the learning rate to be 10^{-4} . The model was trained for 50 epochs.

B. Visual comparison

Fig. 12 and Fig. 13 shows the images reconstructed by the models trained under same dose level. And the corresponding zoomed-in images are displayed in Fig. 14 and Fig. 15.

Fig. 16 and Fig. 17 shows the images reconstructed by the universal models trained for varying dose levels. And the corresponding zoomed-in images are displayed in Fig. 18 and Fig. 19.

See Table VI for quantitative comparison for the results shown in Fig. 12, Fig. 13, Fig. 16 and Fig. 17 .

C. Ablation study

Fig. 20 and Fig. 21 show the images reconstructed by different versions of the AHP-Net trained under same dose level with the dose level of $I_i = 1 \times 10^4$ and $I_i = 5 \times 10^3$. And their zoomed-in images are displayed in Fig. 22 and Fig. 23.

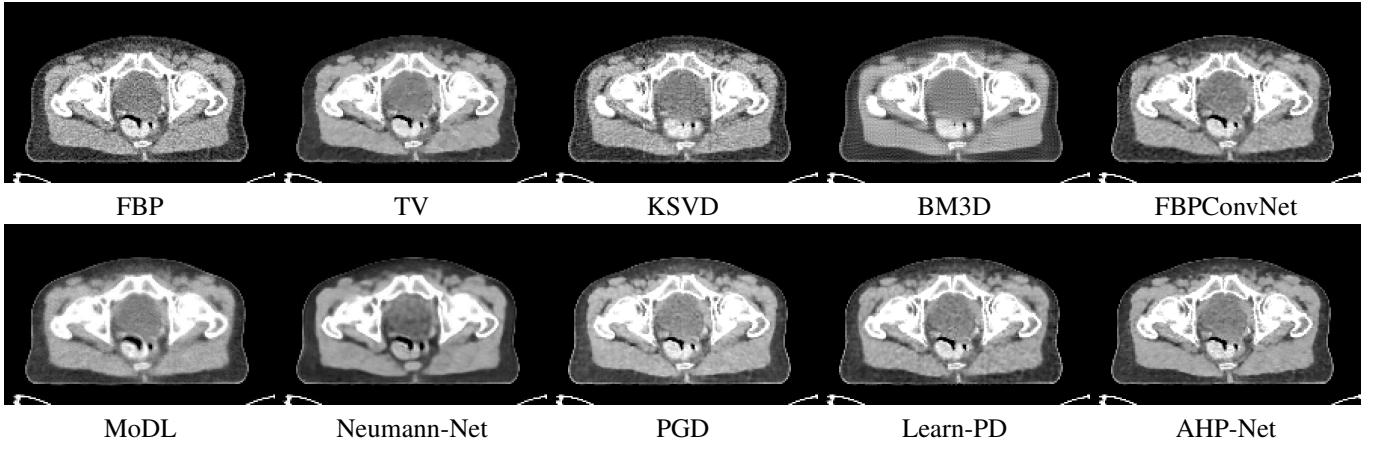


Fig. 12: Reconstruction results at dose level $I_i = 5 \times 10^4$ by the models trained under same dose level.

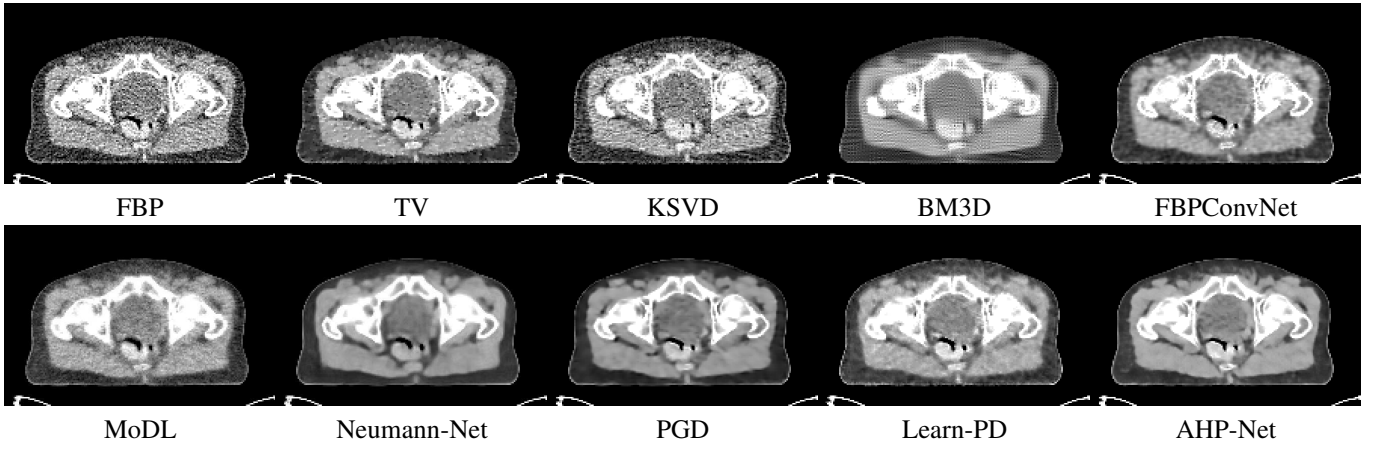


Fig. 13: Reconstruction results at dose level $I_i = 10^4$ by the models trained under same dose level.

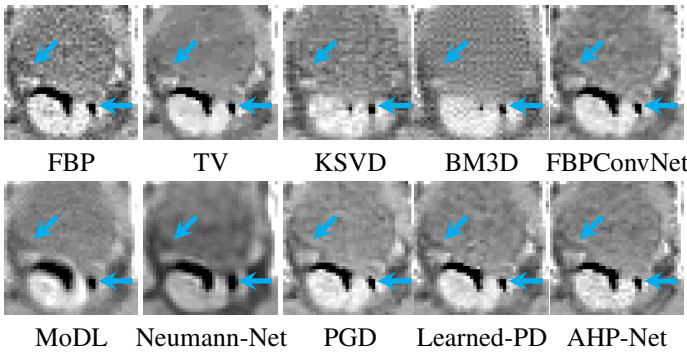


Fig. 14: Zoom-in results of Fig. 12.

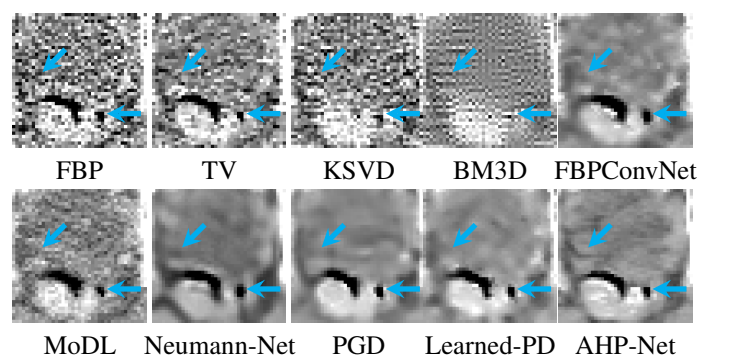


Fig. 15: Zoom-in results of Fig. 13.

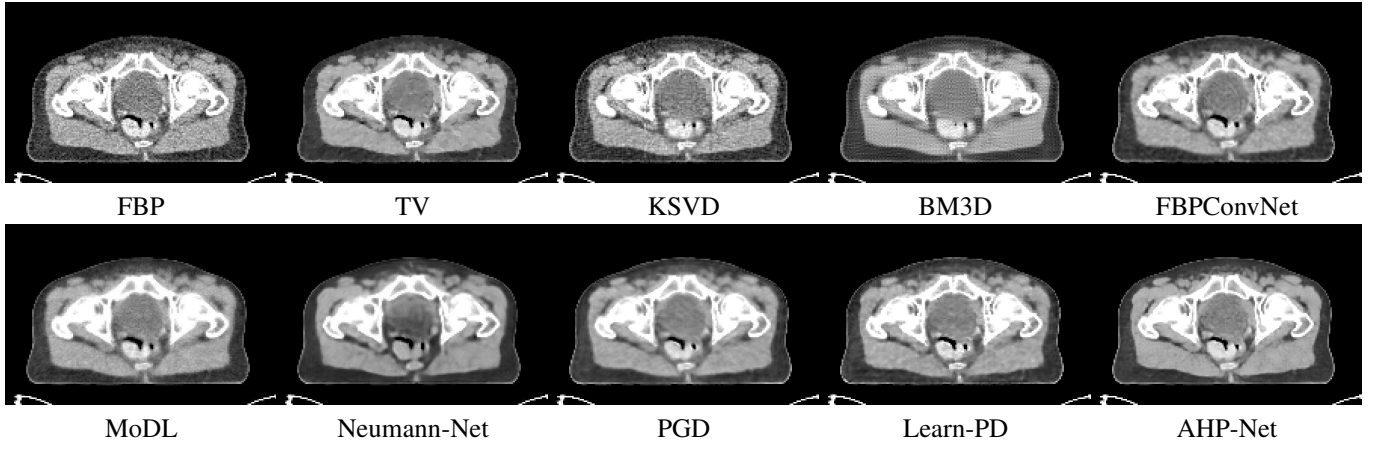


Fig. 16: Reconstruction results at dose level $I_i = 5 \times 10^4$ by the universal models trained for varying dose levels.

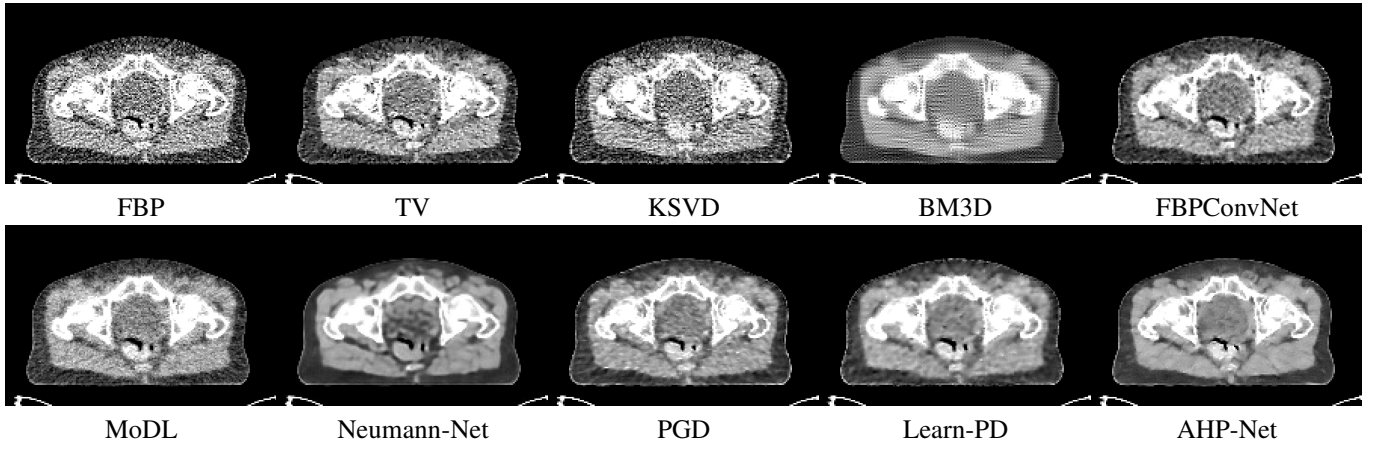


Fig. 17: Reconstruction results at dose level $I_i = 5 \times 10^3$ by the universal models trained for varying dose levels.

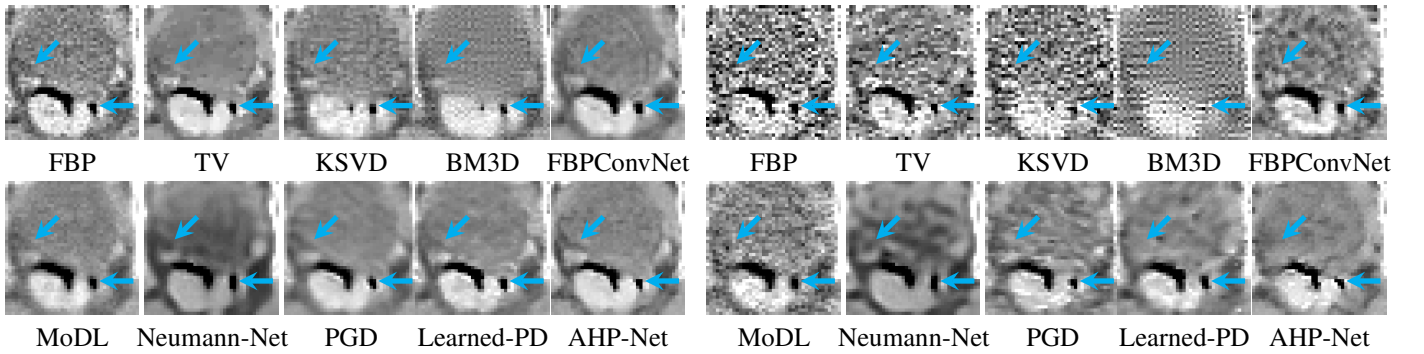


Fig. 18: Zoom-in results of Fig. 16.

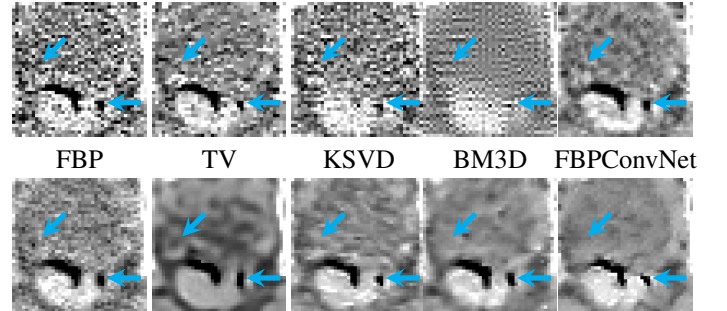


Fig. 19: Zoom-in results of Fig. 17.

TABLE VI: Quantitative metrics on the reconstruction results for the image slice shown in Fig. 12, Fig. 13, Fig. 16 and Fig. 17.

Method	Index	FBP	TV	KSVD	BM3D	FBPCo-nvNet	MoDL	Neuma-nnNet	PGD	Learned-PD	AHP-Net
Fig. 12	PSNR	33.20	35.49	32.34	33.81	34.65	20.98	34.96	35.26	36.04	36.05
	RMSE	22.79	17.50	25.07	21.16	19.29	93.07	18.61	17.99	16.45	15.67
	SSIM	0.9559	0.9752	0.8947	0.9165	0.9638	0.8114	0.9735	0.9341	0.9750	0.9758
Fig. 13	PSNR	28.31	31.65	28.37	29.46	32.00	32.88	31.35	31.83	32.48	34.40
	RMSE	40.03	27.24	39.58	34.91	26.17	23.65	28.22	26.69	24.77	19.85
	SSIM	0.843	0.9355	0.7351	0.8046	0.9437	0.9498	0.9511	0.9300	0.9515	0.9651
Fig. 16	PSNR	33.20	35.50	32.34	33.81	33.45	32.59	33.40	34.30	35.20	37.24
	RMSE	22.79	17.50	25.07	21.16	22.14	24.46	22.28	20.08	18.10	14.31
	SSIM	0.9559	0.9752	0.8947	0.9165	0.9497	0.9356	0.9685	0.9641	0.9714	0.9783
Fig. 17	PSNR	25.12	28.09	25.53	27.42	29.50	30.41	30.92	31.14	30.82	33.34
	RMSE	57.78	41.06	54.90	44.17	34.90	31.44	29.64	28.91	29.97	22.44
	SSIM	0.7278	0.8509	0.6124	0.7267	0.899	0.9143	0.9363	0.9324	0.9322	0.9473



Fig. 20: Reconstruction results at dose level $I_i = 10^4$ by the models trained under same dose level. (a) No filter; (b) Using ∇ ; (c) Learnable filters; (d) Learnable HP; (e) AHP-net.

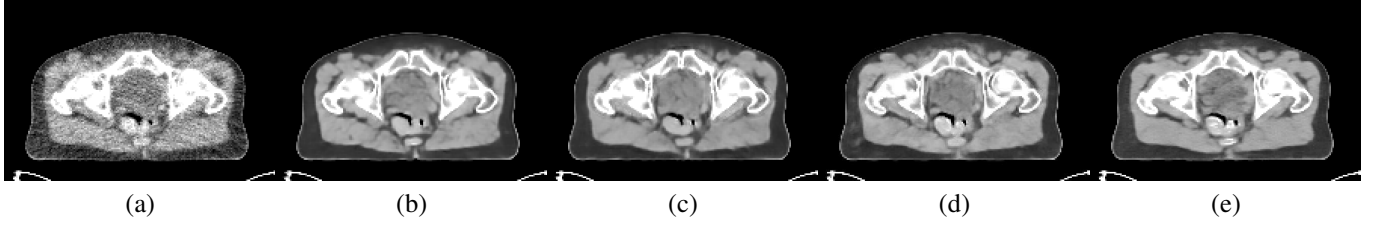


Fig. 21: Reconstruction results at dose level $I_i = 5 \times 10^3$ by the models trained under same dose level. (a) No filter; (b) Using ∇ ; (c) Learnable filters; (d) Learnable HP; (e) AHP-net.

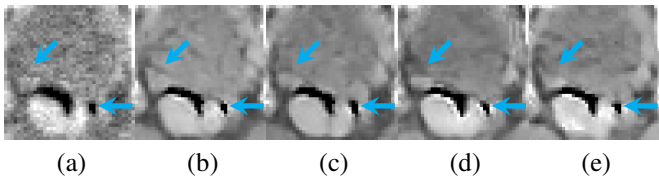


Fig. 22: Zoom-in results of Fig. 20 corresponding to the red boxes in Fig. 4. (a) No Filter; (b) Using ∇ ; (c) Learnable filters; (d) Learnable HP; (e) AHP-net.

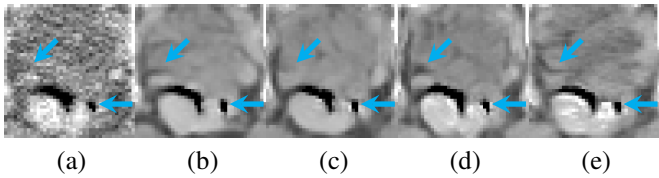


Fig. 23: Zoom-in results of Fig. 21 corresponding to the red boxes in Fig. 4. (a) No Filter; (b) Using ∇ ; (c) Learnable filters; (d) Learnable HP; (e) AHP-net.